



Double-diffusive convection with gravitationally unstable temperature and concentration gradients in homogeneous and heterogeneous porous media

Chenglong Hu^{1,2} and Yantao Yang^{1,2,†}

¹State Key Laboratory for Turbulence and Complex Systems and Department of Mechanics and Engineering Science, College of Engineering, Peking University, Beijing 100871, PR China

²Laoshan Laboratory, Shandong 266299, PR China

(Received 29 April 2024; revised 6 August 2024; accepted 24 September 2024)

Geothermal gradients and heterogeneous permeability are commonly observed in natural geological formations for underground CO₂ sequestration. In this study, we conduct three-dimensional direct numerical simulations on the double-diffusive convection with both unstable temperature and concentration gradients in homogeneous and heterogeneous porous media. For homogeneous porous media, the root-mean-squared velocity increases linearly with density ratio defined as the buoyancy ratio by temperature and concentration differences. The flow structures show no remarkable changes when temperature Rayleigh number Ra_T is less than its critical value, but alter from sheet-like to cellular structures as Ra_T surpasses this threshold. The concentration wavenumber scales approximately as $k_{rS} \sim Ra_e^{0.47}$ with a defined effective Rayleigh number Ra_e . By using a scale analysis, the concentration flux exhibits a consistent linear relation with the total driving forces for all simulations. For heterogeneous porous media, where the Dykstra–Parsons coefficient V_{DP} and correlation length l_r determine the spatial distribution of the permeability field, the flow is strengthened in places with higher permeability. The velocity and concentration flux are less affected by l_r than that by V_{DP} . For small correlation length, the flow structures coarsen and their characteristic width generally increases with increasing heterogeneity. For large correlation length, small structures emerge in the regions with large permeability, which can be attributed to the intensified local Rayleigh number triggering more vigorous convection there. The variations of concentration flux with l_r and V_{DP} can be explained by the portion of area covered by high concentration with large vertical velocity near the boundaries.

Key words: convection in porous media, double-diffusive convection, turbulent convection

† Email address for correspondence: yantao.yang@pku.edu.cn

1. Introduction

Convection in porous media has attracted significant attention in recent decades owing to its huge relevance to geological carbon dioxide (CO₂) sequestration (Ennis-King & Paterson 2003; Riaz & Cinar 2014; Hewitt 2020), which is considered one of the most promising approaches to reduce CO₂ concentration in the atmosphere (Teng & Zhang 2018). In brief, the captured carbon dioxide is compressed into the supercritical state and then injected into deep saline aquifers, typically regarded as porous media saturated with brine at depths greater than 800 m (Bachu 2000). Huppert & Neufeld (2014) has reviewed fluid mechanics involved in this geological sequestration. Upon injection, CO₂ migrates due to buoyancy and partially dissolves into brine, leading to the formation of denser CO₂-saturated brine. Gravity-induced instability at these interfaces further evolves into convection, which in turn increases CO₂ dissolution. The dissolution and convection in porous media are important mechanisms for the stable long-term storage of underground carbon dioxide (Ennis-King & Paterson 2003; Teng & Zhang 2018; Hewitt 2020).

In geological formations, the brine in reservoirs commonly experiences unstable geothermal gradients in a range of 20–65 °C km⁻¹ (Bachu 2003; Nordbotten, Celia & Bachu 2005; Hu, Xu & Yang 2023). Meanwhile, the permeability of porous media is not always homogeneous and has a spatial distribution, which is empirically assumed to be log-normal (Chen, Zeng & Shi 2013). The present study consists of three-dimensional (3-D) numerical simulations of double-diffusive convection (DDC) with both gravitationally unstable temperature and concentration gradients. Both homogeneous and heterogeneous permeability are investigated. The principal objectives are to reveal the influences of geothermal gradients and heterogeneous permeability on flow structures and concentration transfer.

The underground reservoirs are modelled by two parallel horizontal plates, representing impermeable cap rock layers, with saturated porous media inside. Two typical configurations of boundary conditions have been applied in previous studies of single-phase convective dissolution in porous media (Hewitt 2020). One is time-evolving one-sided convection with a fixed concentration at the top and no concentration flux at the bottom, commonly referred to as convective dissolution. The other is statistically stable two-sided convection with fixed temperature (or concentration) at the upper and lower boundaries, commonly known as Rayleigh–Darcy convection (RDC) or single-component convection. In homogeneous porous media, transient behaviours of convective fingers and variations of concentration flux over time have been studied extensively in one-sided convection (Xu, Chen & Zhang 2006; Hewitt, Neufeld & Lister 2013). The dissolution rate is categorised into different regimes as time progresses (Slim 2014), and eventually enters a decaying shutdown regime (Hewitt *et al.* 2013). Two-sided convection focuses on the influence of driving force, i.e. Rayleigh number Ra , on dominant flow structures and heat (or concentration) flux. Previous studies have revealed that the scaling between the flux Nu and Ra varies across different Ra ranges. Otero *et al.* (2004) conducted two-dimensional (2-D) numerical simulations and found $Nu \sim Ra$ over an intermediate range $50 \lesssim Ra \lesssim 1200$ and $Nu \sim Ra^{0.9}$ from 1255 to 10^4 . Hewitt, Neufeld & Lister (2012) found a similar scaling $Nu \sim Ra^{0.95}$ in high- Ra range $1300 \lesssim Ra \leq 4 \times 10^4$ in 2-D simulations. Later, Hewitt, Neufeld & Lister (2014) extended simulations to 3-D cases and observed a fitted linear scaling $Nu = 0.0096Ra + 4.6$ in the range $1750 \leq Ra \leq 2 \times 10^4$. More recently, Pirozzoli *et al.* (2021) and De Paoli *et al.* (2022) have pushed Rayleigh number up to a large value of 8×10^4 , adding a sublinear corrective term that only influences moderate Ra values. Zhu, Fu & De Paoli (2024) proposed a possible explanation for this additional nonlinear term. The size of flow structures can be measured by the wavenumber, which

follows a fitted scaling $Ra^{0.4}$ in 2-D simulations (Hewitt *et al.* 2012) and approximately $Ra^{0.5}$ in 3-D simulations (Hewitt *et al.* 2014; De Paoli *et al.* 2022).

Early studies of DDC in homogeneous porous media focused on the onset of convection. Using linear stability analysis, Nield (1968) obtained critical Rayleigh numbers and corresponding critical wavenumbers under various boundary conditions of temperature and concentration. Taunton, Lightfoot & Green (1972) extended the analysis to determine conditions for salt fingers. Anisotropic permeability and diffusion coefficients were further considered by Tyvand (1980) to investigate thermohaline instability. The above studies used Darcy's law to determine the seepage velocity. Instability of flows described by a Brinkman model has also been explored (Wang & Tan 2009; Prakash & Gupta 2012). In numerical simulations, Trevisan & Bejan (1987) considered the buoyancy effect solely by temperature gradient in 2-D porous media and obtained a scaling law of mass transfer rate for various Lewis numbers. Laboratory experiments were carried out by Griffiths (1981) who measured the heat and salt fluxes through interfaces in a two-layer convecting system in a Hele-Shaw cell. Murray & Chen (1989) considered the onset of DDC in a finite box of porous medium. Persistent investigations into DDC in porous media encompass various aspects, including horizontal throughflow (Rubin & Roth 1979), vertical vibration (Jounet & Bardan 2001), mechanical dispersion (Rosenberg & Spera 1992), heat-releasing concentration (Hill 2005) and nonlinear stability (Lombardo, Mulone & Straughan 2001). Comprehensive reviews of DDC in porous media have been conducted by Trevisan & Bejan (1990), Vafai (2005) and Nield & Bejan (2017). In our recent study (Hu *et al.* 2023), we systematically investigated the effects of unstable geothermal gradients on the one-sided convection. It has been addressed that large-scale rolls induced by the geothermal gradient can significantly influence flow structures and dissolution rates. The long-term variation of dissolution flux over time exhibits consistent decaying behaviour and can be modelled by a theoretical relation.

Another important factor to consider is permeability heterogeneity quantified by the Dykstra–Parsons coefficient V_{DP} , which ranges from 0, indicating perfect homogeneity, to 1, signifying maximum heterogeneity. Buoyancy-driven convection in heterogeneous porous media has been investigated theoretically, numerically and experimentally. The effects of heterogeneity on the onset of convection in porous media have been discussed extensively in a series of studies (Nield & Kuznetsov 2007*a,b*; Nield, Kuznetsov & Simmons 2010; Nield & Kuznetsov 2011). Braester & Vadasz (1993) utilised a perturbation expansion method to study weak heterogeneity. Heterogeneous permeability can be generated by many methods. For instance, Soboleva (2018) introduced inhomogeneity using multiple horizontal layers at different porosity and permeability. Mahyapour *et al.* (2022) employed the sequential Gaussian simulation method to produce random permeability fields and studied the effects of permeability heterogeneity on one-sided convective dissolution. Farajzadeh *et al.* (2010) used spectral methods to generate 2-D fields with various correlation lengths and V_{DP} . They concluded three flow regimes (fingering, dispersive and channeling) for density-driven natural convection flow through numerical simulations, which adopts the ideas of Waggoner, Castillo & Lake (1992), and found the heterogeneity is not related to the mass of dissolved CO_2 . Similar results were given by Ranganathan *et al.* (2012). However, an increase in total dissolved CO_2 with heterogeneity was observed by Kong & Saar (2013). Experimental set-ups include a sloping permeability jump in a saturated two-layered porous medium (Bharath & Flynn 2021), a Hele-Shaw cell with a thin horizontal layer of circular impermeable discs (Salibindla *et al.* 2018) and packed stratified plastic resin particles with different average diameter (Wang *et al.* 2017). As for DDC, Kuznetsov & Nield (2008, 2012) analytically

studied the onset of convection using linear stability theory. Islam, Lashgari & Sephernoori (2014*b*) numerically investigated 2-D convective dissolution with geothermal gradients. Results revealed that dissolution is enhanced with increasing both solutal Rayleigh number and heterogeneity level, and the geothermal effect has a minor effect on overall dissolution process.

The rest of the paper is organised as follows. In § 2, we describe the governing equations and corresponding numerical methods, as well as the control parameter spaces and methods for generating heterogeneous permeability fields. In § 3, we analyse numerical results of DDC in homogeneous porous media, including flow structures and fluxes. In § 4, we focus on variations of permeability heterogeneity in both RDC and DDC. Finally, we summarise our results in § 5.

2. Methodology

2.1. Governing equations

In a Cartesian coordinate $\mathbf{x} = (x, y, z)$, we consider a 3-D cell containing fluid-saturated porous media bounded by two horizontal plates with a uniform porosity ϕ . The cell has a height of H , and its length and width are both L . The permeability of porous media is either homogeneous, characterised by a constant value \bar{K} , or heterogeneous, defined by a spatial function $K(\mathbf{x}) = \bar{K}f(\mathbf{x})$ following a certain distribution. Here $f(\mathbf{x})$ is a normalised function to describe permeability heterogeneity, with an average value of unity over the entire domain. Note that the permeability is generally considered a second-order tensor with anisotropy in the horizontal and vertical directions (Rapaka *et al.* 2009; Green & Ennis-King 2014; De Paoli, Zonta & Soldati 2017; Nield & Bejan 2017). For simplicity, we assume isotropic permeability in this study. The details of generating a heterogeneous permeability field are discussed in the following section. The cell is maintained at a constant concentration at the top and zero concentration at the bottom. Meanwhile, there is a consistent unstable geothermal gradient across the domain against the direction of gravity. In other words, the saturated porous media are heated from below and cooled from above. We denote concentration and temperature as S and T , respectively. The top and bottom boundaries are marked with subscripts ‘*top*’ and ‘*bot*’, respectively. The density of fluid follows a linear relation as $\rho = \rho_0[1 - \beta_T(T - T_{top}) + \beta_S(S - S_{bot})]$, where β_T and β_S are linear coefficients of expansion and ρ_0 is a reference value. The governing equations of an incompressible Darcian flow with both heat and mass transfer read

$$\nabla \cdot \mathbf{u} = 0, \tag{2.1a}$$

$$\mathbf{u} = -\frac{K(\mathbf{x})}{\mu}[\nabla p + (\beta_S S - \beta_T T)\rho_0 g \mathbf{e}_z], \tag{2.1b}$$

$$\frac{(\rho c)_m}{(\rho c)_f} \frac{\partial T}{\partial t} = -\mathbf{u} \cdot \nabla T + \kappa_m \nabla^2 T, \tag{2.1c}$$

$$\phi \frac{\partial S}{\partial t} = -\mathbf{u} \cdot \nabla S + \phi \kappa_S \nabla^2 S. \tag{2.1d}$$

Here \mathbf{u} is the seepage velocity, p is the pressure, g is the gravitational acceleration, \mathbf{e}_z is the vertical unit vector opposite to direction of gravity, μ is fluid viscosity, $(\rho c)_m$ is the overall heat capacity of solid and fluid, $(\rho c)_f$ is the heat capacity of fluid, κ_m is the overall thermal diffusivity and κ_S is the molecular diffusivity of concentration field, respectively. The subscript ‘*m*’ represents the combination of both the solid matrix and saturated fluid, whereas ‘*f*’ represents the fluid alone. Note that local thermal equilibrium is assumed in

Double-diffusive convection

(2.1c). Periodicity is imposed on the horizontal directions, namely, the x and y dimensions, for all variables. The boundary conditions at the bottom and top boundaries are

$$u_z = 0, \quad T = T_{bot}, \quad S = S_{bot}, \quad \text{at } z = 0, \quad (2.2a)$$

$$u_z = 0, \quad T = T_{top}, \quad S = S_{top}, \quad \text{at } z = H. \quad (2.2b)$$

The above governing equations are non-dimensionalised by the height H , the temperature difference $\Delta T = T_{bot} - T_{top}$, the concentration difference $\Delta S = S_{top} - S_{bot}$, the characteristic velocity $U_c = \bar{K}g\rho_0\beta_S\Delta S/\mu$, and the characteristic time scale $t_c = \phi H/U_c$, respectively. Then the non-dimensionalised equations are

$$\nabla \cdot \mathbf{u} = 0, \quad (2.3a)$$

$$\mathbf{u} = [-\nabla p + (\Delta T - S)\mathbf{e}_z]f(\mathbf{x}), \quad (2.3b)$$

$$\sigma \frac{\partial T}{\partial t} = -\mathbf{u} \cdot \nabla T + \frac{Le}{Ra_S} \nabla^2 T, \quad (2.3c)$$

$$\frac{\partial S}{\partial t} = -\mathbf{u} \cdot \nabla S + \frac{1}{Ra_S} \nabla^2 S. \quad (2.3d)$$

In the remainder of this article, all variables are dimensionless unless otherwise mentioned. Note that both the temperature and concentration differences are positive, which means the two scalars simultaneously drive convective motions.

There are four dimensionless control parameters in the above equations, including the heat capacity ratio σ , the Lewis number Le , the concentration Rayleigh number Ra_S and the temperature Rayleigh number Ra_T , which are respectively defined as

$$\sigma = \frac{(\rho c)_m}{\phi(\rho c_p)_f}, \quad Le = \frac{\kappa_m}{\phi\kappa_S}, \quad Ra_S = \frac{\bar{K}Hg\rho_0\beta_S\Delta S}{\kappa_S\mu\phi}, \quad Ra_T = \frac{\bar{K}Hg\rho_0\beta_T\Delta T}{\kappa_m\mu}. \quad (2.4a-d)$$

The density ratio $\Lambda = (\beta_T\Delta T)/(\beta_S\Delta S) = Ra_T Le/Ra_S$ can be assembled to measure the strength of the temperature difference relative to the concentration difference. The non-dimensionalised boundary conditions at the bottom and top boundaries then become

$$u_z = 0, \quad T = 1, \quad S = 0, \quad \text{at } z = 0, \quad (2.5a)$$

$$u_z = 0, \quad T = 0, \quad S = 1, \quad \text{at } z = 1. \quad (2.5b)$$

2.2. Permeability heterogeneity

Before solving the governing equations, the heterogeneous permeability field must be properly generated as a reflection of realistic geological formations. Permeability in natural geological formations is empirically assumed to follow a log-normal distribution. Thus, the normalised permeability function $f(\mathbf{x})$ is modelled by the exponential of a random Gaussian field $G(\mathbf{x})$ which has zero mean and unit standard deviation (Oliver 1995; Camhi, Meiburg & Ruith 2000; Abrahamsen, Kvernelv & Barker 2018). The autocovariance function of $G(\mathbf{x})$ is given as $C(\mathbf{x}) = \exp(-(x/l_r)^2)$ where l_r denotes the non-dimensionalised correlation length. We use the Dykstra–Parsons coefficient V_{DP} to measure the strength of heterogeneity. When permeability is log-normally distributed, V_{DP} can be expressed as $V_{DP} = 1 - e^{-s_{\ln k}^2}$, where $s_{\ln k}$ is the standard deviation of logarithmic $f(\mathbf{x})$ (Kong & Saar 2013). Consequently, the normalised permeability function $f(\mathbf{x})$ can be

expressed as

$$f(\mathbf{x}) = \exp\left(-\frac{s_{\ln k}^2}{2} + s_{\ln k}G\right). \quad (2.6)$$

2.3. Numerical details

To numerically solve the governing equations (2.3) with boundary conditions (2.5), we first take the divergence of (2.3b) and combine it with continuity equation (2.3a). An equation for pressure can be obtained as

$$\nabla \cdot (f\nabla p) = \frac{\partial}{\partial z}[(\Delta T - S)f], \quad (2.7)$$

with boundary conditions as

$$\left.\frac{\partial p}{\partial z}\right|_{z=0,1} = (\Delta T - S)|_{z=0,1}. \quad (2.8)$$

For homogeneous porous media, $f(\mathbf{x})$ equals one in the entire domain. Equation (2.7) reduces into a Poisson's equation, which can be solved by the same numerical method as described in Hu *et al.* (2023). Specifically, apply Fourier transform in the horizontal directions and solve a set of tridiagonal systems in the vertical direction. However, $f(\mathbf{x})$ becomes spatially dependent when considering heterogeneity. Equation (2.7) is generally a Poisson's equation with variable coefficients and can no longer be solved by a fast direct algorithm. Therefore, an iterative V-cycle multigrid method is employed (Briggs, Henson & McCormick 2000). The iteration stops when the divergence of velocity field is less than 10^{-6} . After solving the pressure field, the velocity can be calculated using (2.3b). The advection–diffusion equations for temperature and concentration can then be solved by the scheme described in Ostilla-Mónico *et al.* (2015). Initially, the concentration and temperature fields have vertically linear distributions based on their boundary values.

In this study, the Lewis number and heat capacity ratio are fixed at $Le = 100$ and $\sigma = 1$, respectively. The parameter spaces are shown in figure 1. For homogeneous porous media, we explore four concentration Rayleigh numbers ranging from 10^3 to 10^4 and six temperature Rayleigh numbers ranging from zero, i.e. without geothermal gradient, to 300. The Rayleigh numbers fall within ranges estimated by Hu *et al.* (2023) for realistic conditions in CO₂ sequestration, with the concentration Rayleigh number up to 10^5 and the temperature Rayleigh number as high as 10^3 . For heterogeneous cases, we fix the concentration Rayleigh number at 10^3 and the temperature Rayleigh numbers at zero or 50. The two parameters concerning heterogeneity are correlation length l_r , ranging from 0.1 to 1.0, and the Dykstra–Parsons coefficient V_{DP} , ranging from 0.1 to 0.6. Previous studies on permeability heterogeneity in porous media in the context of CO₂ sequestration have considered various ranges of the Dykstra–Parsons coefficient and correlation length (Waggoner *et al.* 1992; Jensen *et al.* 1997; Camhi *et al.* 2000; Farajzadeh *et al.* 2010; de Dreuzy *et al.* 2012; Ranganathan *et al.* 2012; Kong & Saar 2013; Islam *et al.* 2014a,b). To conclude, V_{DP} and l_r vary in the ranges $0.01 \leq V_{DP} \leq 0.9$ and $0.01 \leq l_r \leq 3$, respectively. Therefore, the parameters explored in this study are representative of realistic conditions.

3. Homogeneous porous media

In the context of convection in homogeneous porous media, our major concern is how the geothermal gradient influences flow dynamics and transport properties compared with

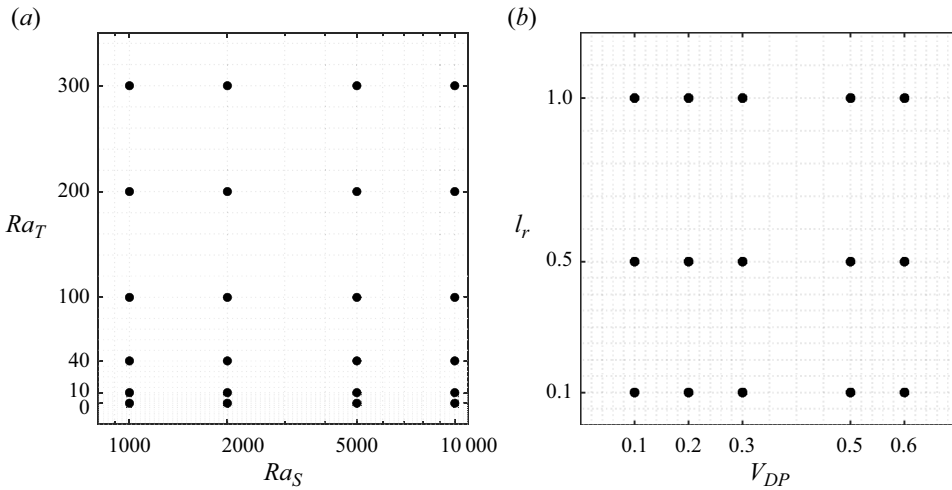


Figure 1. Parameter spaces for (a) homogeneous and (b) heterogeneous porous media. Note that we set $Ra_S = 10^3$ and $Ra_T = 0$ or 50 in heterogeneous porous media.

convection in the absence of such a gradient. To examine such influences, we conduct numerical simulations in the concentration Rayleigh number range $10^3 \leq Ra_S \leq 10^4$. For each Ra_S , the temperature Rayleigh number ranges from $0 \leq Ra_T \leq 300$. Note that the critical Rayleigh number for single-component RDC is $Ra_{cr} = 4\pi^2$ (Lapwood 1948), which is slightly less than 40. An instinctual assumption is that the temperature gradient barely influences the flow when Ra_T is less than Ra_{cr} . In this circumstance, temperature is more like a passive scalar driven by concentration convective motions.

3.1. Alternation of flow structures

3.1.1. Root-mean-square of velocity field u^{rms}

We first look at the time- and volume-averaged root-mean-square (r.m.s.) of velocity field u^{rms} as shown in figure 2. The observation in figure 2(a) is evident that u^{rms} shows no significant change for $Ra_T = 0$ and 10 regardless of Ra_S . However, when considering a constant concentration Rayleigh number, u^{rms} demonstrates an approximately linear escalation with increasing Ra_T for values exceeding 40. It is noteworthy that the slope differs for various Ra_S values. For clarification, the observed decrease in u^{rms} with increasing Ra_S at a fixed temperature Rayleigh number is due to the non-dimensionalisation of variables used in our study. The dimensional velocity should increase with stronger driving forces. Exploring the variations of u^{rms} with the density ratio Δ , we observe a consistent linear trend in the data with respect to Δ . A linear best-fit model of $u^{rms} = 0.115(\Delta + 1)$ is also depicted in figure 2(b). Such a linear tendency can be explained by the fact that the total driving forces of convection include density differences induced by both concentration and temperature differences. However, only concentration difference is used when non-dimensionalising the governing equations, resulting in a $(\Delta + 1)$ term for the non-dimensionalised u^{rms} .

Recently, Zhu *et al.* (2024) have presented a theoretical relation for the r.m.s. of velocity u^{rms} (or the corresponding Péclet number Pe), the Nusselt number Nu and the Rayleigh number Ra in single-component convective porous media flows. Similarly, we can obtain a relation in the double-diffusive scenario for u^{rms} , the Nusselt and Rayleigh numbers,

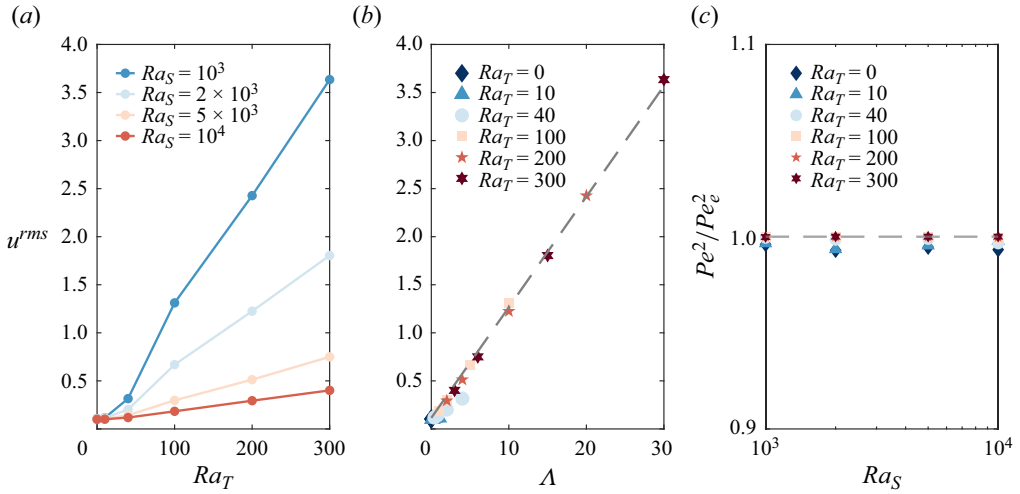


Figure 2. Root-mean-square of time- and volume-averaged velocity varies with (a) temperature Rayleigh number Ra_T and (b) density ratio Λ . The grey dashed line in (b) is a linear fit $u^{rms} = 0.115(\Lambda + 1)$. The ratio of Péclet number Pe to its analytical relation Pe_e against Ra_S is plotted in (c), with the grey dashed line indicating unity value.

which reads

$$Pe^2 = Ra_S[\Lambda Le(Nu_T - 1) + (Nu_S - 1)], \quad (3.1)$$

where $Pe = Ra_S u^{rms}$. The derivation details are provided in Appendix B. The ratio of numerical measurements to the theoretical relation is depicted in figure 2(c). The results demonstrate excellent agreement between the measurements and theory, both for $Ra_T = 0$ and for $Ra_T > 0$.

3.1.2. Structures of the flow

The flow structures exhibit variations with concentration and temperature Rayleigh numbers. Figure 3 presents horizontal slices of vertical velocity, concentration, and temperature at $z = 0.5$ for two concentration Rayleigh numbers. To analyse the impacts of different temperature gradients, the subfigures are organised in descending rows corresponding to increasing Ra_T . For a fixed Ra_S , it is notable that only when Ra_T is greater than 40 do the flow structures alter significantly. When $Ra_T = 0$ and 10, the concentration field comprises randomly distributed column-like structures of comparable size. In other words, the flow is almost unaffected if $Ra_T < Ra_{cr}$, aligning with the aforementioned assumption. However, as Ra_T surpasses Ra_{cr} , either concentration or temperature difference can independently drive convection, while their combined effect leads to more intricate flow patterns. The concentration field displays sheet-like structures and cellular structures with elongated borders where concentration reaches maximum or minimum. The interfaces of concentration structure in horizontal directions become more distinct as Ra_T increases for a fixed Ra_S when $Ra_T > Ra_{cr}$ (see figure 3c–e).

It is worth noting that the temperature structures display variations at an identical Ra_T when the concentration Rayleigh number differs. This suggests that the density ratio also influences the flow structures. For instance, when $Ra = 10^3$ and $Ra_T = 100$ (density ratio corresponding to $\Lambda = 10$), parallel sheet-like structures prevail in the left panel of figure 3(d). The temperature field is similar to convection solely driven by temperature

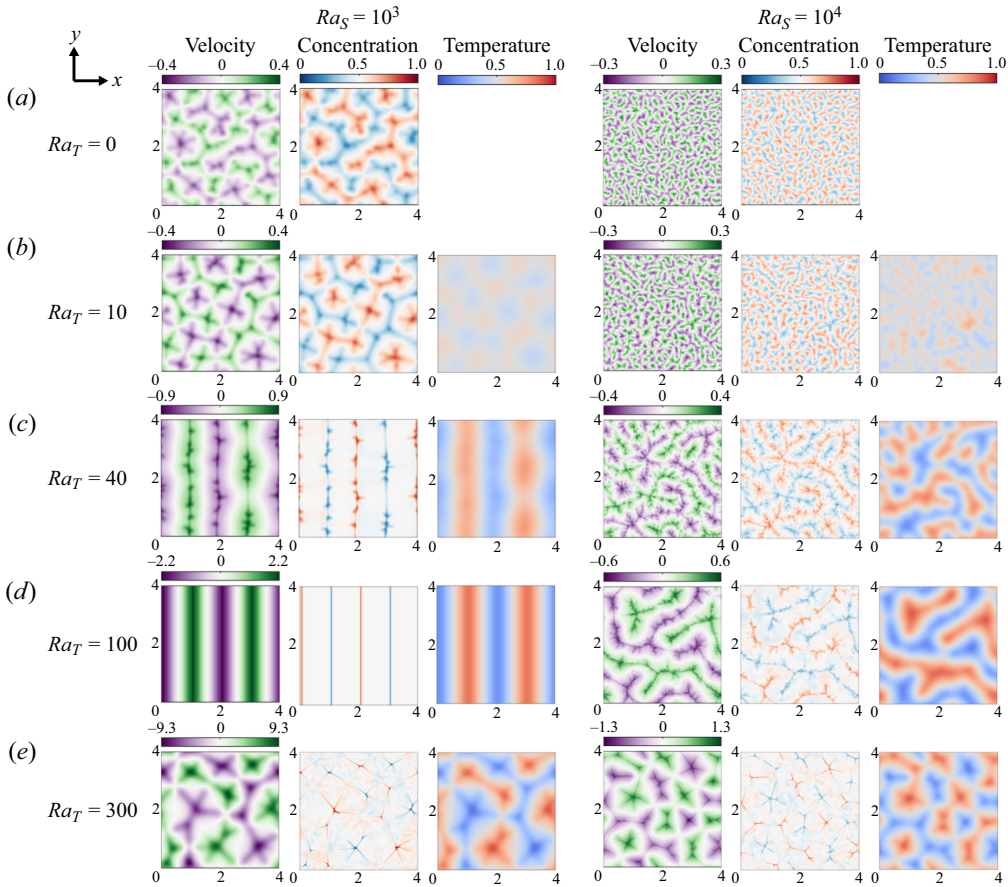


Figure 3. Horizontal slices of vertical velocity, concentration and temperature at $z = 0.5$. The left three columns correspond to $Ra_S = 10^3$, and the right three columns to $Ra_S = 10^4$. Each row represents a temperature Rayleigh number, ranging from (a) 0 to (e) 300.

at $Ra_T = 100$. However, when $Ra = 10^4$ and $Ra_T = 100$ (density ratio corresponding to $\Lambda = 1$), parallel sheets break down and reorganise. This is due to the differing relative strengths of buoyancy induced by temperature and concentration. In the former case, $\Lambda = 10$ indicates the flow is primarily driven by temperature difference, resulting in structures similar to those solely driven by $Ra_T = 100$. In the latter case, the buoyant forces from concentration and temperature are equivalent, leading to deviations from structures of RDC driven by either $Ra_S = 10^4$ or $Ra_T = 100$.

Furthermore, upon comparing temperature and concentration slices under identical control parameters, it is evident that concentration structures typically concentrate in the centre of corresponding temperature structures, where the vertical velocity attains its maximum. This observation implies high concentration can be transported quickly from the top plate to the bottom in these areas and *vice versa*. To further illustrate such implications, vertical slices of concentration at $y = 0.5L$ for $Ra_S = 10^4$ are presented in figure 4. For large Ra_T , the concentration structures consist of numerous short fingers emerging from the boundaries and a few long plumes extending across the entire vertical direction, reflecting the footprints of large-scale rolls induced by temperature. As Ra_T increases, more and more concentration fingers are confined within a short vertical

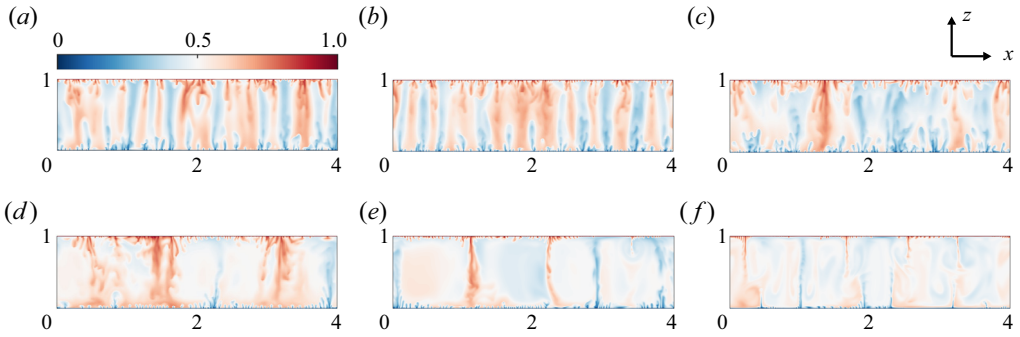


Figure 4. Vertical slices of concentration at $y = 0.5L$ for $Ra_S = 10^4$: (a) $Ra_T = 0$, (b) $Ra_T = 10$, (c) $Ra_T = 40$, (d) $Ra_T = 100$, (e) $Ra_T = 200$ and (f) $Ra_T = 300$.

distance apart from the top and bottom boundaries, and the plumes become thinner. In addition, mixing is enhanced and concentration is more homogenised in the bulk region for increasing temperature gradient.

The horizontal slices in figure 3 indicate that the structure sizes vary with the Rayleigh numbers. The size of dominant structures is typically quantified by the mean radial wavenumber at the centre plane $z = 0.5$. Consider a 2-D power spectrum of the concentration slice at $z = 0.5$, $E(k_x, k_y)$, where k_x and k_y are the wavenumbers in the x and y directions, respectively. The time-averaged radial wavenumber for concentration is defined as

$$k_{rS} = \left\langle \frac{\iint \sqrt{k_x^2 + k_y^2} E(k_x, k_y) dk_x dk_y}{\iint E(k_x, k_y) dk_x dk_y} \right\rangle. \quad (3.2)$$

In 3-D RDC, numerical measurements have provided fitted scalings of $k_r \approx 0.17Ra^{0.52}$ by Hewitt *et al.* (2014) and $k_r \approx 0.25Ra^{0.49}$ by De Paoli *et al.* (2022). In figure 5(a), we present the variations of k_{rS} with both concentration and temperature Rayleigh numbers. Results from De Paoli *et al.* (2022) are also included for comparison, showing good agreement with our results at $Ra_T = 0$. For the case $Ra_T = 10$, k_{rS} is nearly the same as for $Ra_T = 0$ at a fixed Ra_S . However, when $Ra_T \geq 40$, the wavenumber does not follow the approximate 1/2 power scaling with Ra_S . Here, we define an effective Rayleigh number Ra_e to indicate the total driving buoyant forces of both concentration and temperature as

$$Ra_e \equiv Ra_S + LeRa_T = Ra_S(1 + \Lambda). \quad (3.3)$$

After plotting k_{rS} against Ra_e in a logarithmic coordinate in figure 5(b), we find that the averaged radial wavenumber exhibits a linear increase with the effective Rayleigh number. The best data fitting results in

$$k_{rS} \approx 0.23Ra_e^{0.47}. \quad (3.4)$$

The fitting exponent and coefficient are close to the fitted scaling by De Paoli *et al.* (2022). Although our numerical measurements do not perfectly collapse on the best-fit line, the fitted scaling successfully captures the trend of structure size varying with the Rayleigh numbers.

Double-diffusive convection

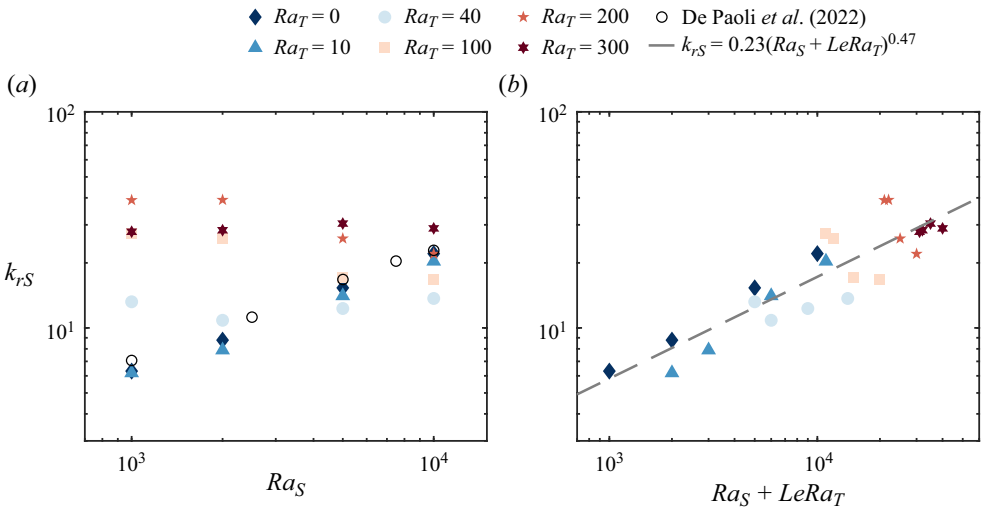


Figure 5. The mean radial wavenumber $k_{r,S}$ of concentration field at $z = 0.5$ against (a) the concentration Rayleigh number Ra_S and (b) the effective Rayleigh number $Ra_e = Ra_S + LeRa_T$. The black empty circles in (a) represent 3-D numerical results from De Paoli *et al.* (2022) in single-component RDC. The grey dashed line in (b) is the best power fit $k_{r,S} = 0.23Ra_e^{0.47}$.

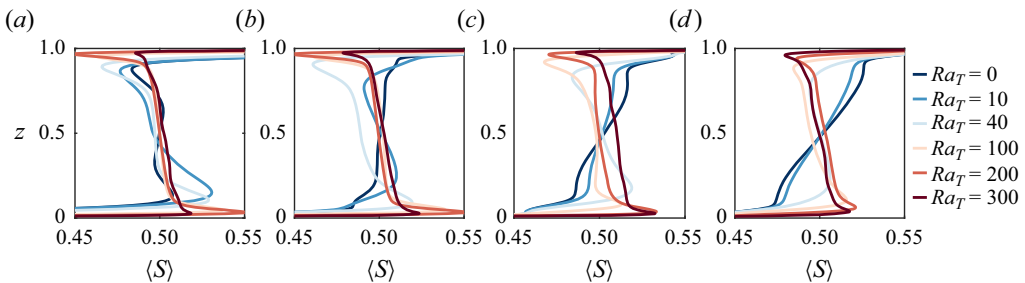


Figure 6. Concentration mean profiles: (a) $Ra_S = 10^3$, (b) $Ra_S = 2 \times 10^3$, (c) $Ra_S = 5 \times 10^3$ and (d) $Ra_S = 10^4$. Line colours from blue to red represent increasing temperature Rayleigh number.

3.1.3. Concentration mean profiles

In figure 6 we plot the concentration mean profiles for all cases in the parameter space. The symbol angle brackets stand for an average over time and (x, y) planes. For each profile, there are two distinct boundary layers near the top and bottom plates, and the concentration is approximately linear with height in the bulk regions around the centre. For a fixed Ra_S , the thickness of boundary layers decreases and the concentration gradient near the centre changes from positive to negative with increasing Ra_T . We measure the concentration gradient G_S in the range $0.4 \leq z \leq 0.6$ and plot its dependence on Ra_S and Ra_T in figure 7. Then G_S becomes negative when Ra_T is larger than 40 for all explored Ra_S . In other words, the concentration gradient in the bulk is opposite to that imposed on the vertical boundaries provided that Ra_T exceeds the critical Ra_{cr} . Such a phenomenon can be attributed to the fact that increasing Ra_T for a fixed Ra_S is equivalent to increasing density ratio, resulting in a higher vertical velocity. Flow with high vertical velocity can transfer high concentration quickly from the top to the bottom with little diffusion, and *vice versa*. Consequently, the concentration gradient in the bulk becomes negative. A positive value of the concentration

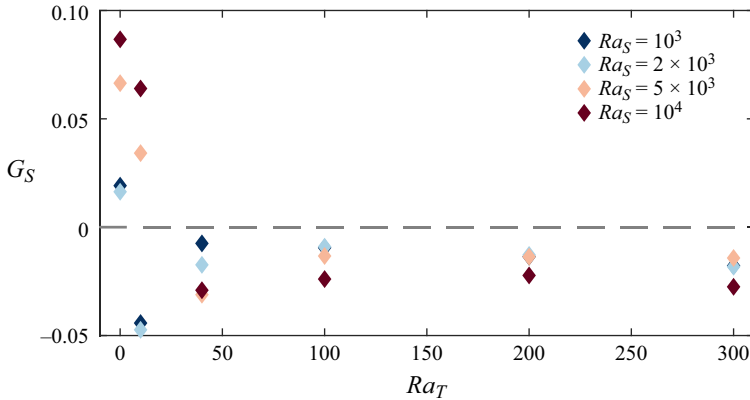


Figure 7. Concentration gradient calculated in the range $0.4 \leq z \leq 0.6$.

gradient is expected at low Ra_T . However, it is noteworthy that the minimum G_S occurs at $Ra_T = 10$ with two lower concentration Rayleigh numbers, $Ra_S = 10^3$ and 2×10^3 . In the context of RDC, De Paoli *et al.* (2022) reported similar counter-gradient flux regions at the edge of thermal boundary layer at small Rayleigh numbers ($Ra = 10^3$ in their cases), ascribing this phenomenon to vertical plumes that carry their momentum and temperature almost unchanged across the fluid layer. These regions tend to diminish with increasing Ra . Based on our current numerical results, we can only offer a qualitative description of this phenomenon rather than a definitive explanation. In our cases, although only a very small Ra_T is introduced at $Ra_S = 10^3$ and 2×10^3 , the nonlinear interaction between concentration and temperature results in extending the counter-gradient flux regions into the bulk and can significantly invert the concentration gradient.

3.2. Variation of fluxes with Ra_S and Ra_T

The non-dimensionalised concentration flux is defined as the mean value of the vertical concentration gradient at the top and bottom boundaries:

$$Nu_S = \frac{1}{2} \left(\left\langle \frac{\partial S}{\partial z} \right|_{z=0} + \frac{\partial S}{\partial z} \Big|_{z=1} \right), \quad (3.5)$$

where $\langle \cdot \rangle$ denotes averaging over time and horizontal directions. The definition of the heat flux Nu_T is similar. Previous studies have analysed heat or concentration transfer in 3-D single-component RDC and concluded a nearly linear scaling law $Nu \sim \alpha_0 Ra$ at high Rayleigh numbers in the range $1750 \leq Ra \leq 2 \times 10^4$ with the linear coefficient α_0 around 0.01 (Hewitt *et al.* 2014). However, it is not always the case when considering an additional aiding temperature gradient.

3.2.1. Numerical measurements

The variance of concentration flux with Ra_S and Ra_T is shown in figure 8. In figure 8(a), for the cases $Ra_T = 0, 10, 40$, the linear relation can still retain for the Ra_S range we explored and their curves almost collapse. For comparison, the linear relation $Nu_S = 0.0096Ra_S + 4.6$ given by (Hewitt *et al.* 2014) is also depicted in figure 8(a). This indicates that when the temperature Rayleigh number is small, it merely influences concentration flux. However, for the cases $Ra_T = 100, 200$ and 300 , the variations with Ra_S are clearly

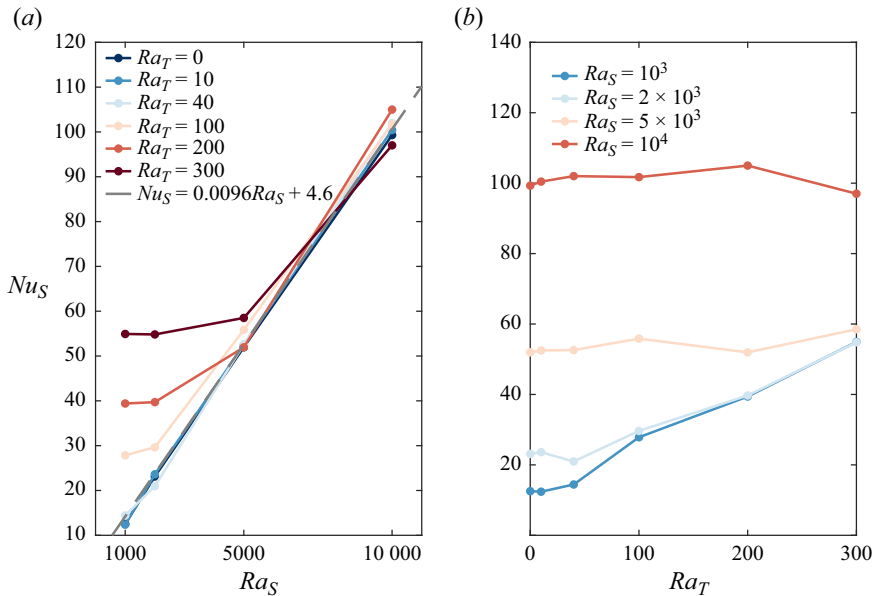


Figure 8. The variance of concentration flux with (a) concentration Rayleigh number and (b) temperature Rayleigh number. The grey dashed line in (a) indicates a linear relation obtained by Hewitt *et al.* (2014) in 3-D RDC.

nonlinear, with an elevation at two smaller concentration Rayleigh numbers $Ra_S = 10^3$ and 2×10^3 . In figure 8(b), the fluxes for two higher Ra_S do not change significantly. However, for two lower $Ra_S = 10^3$ and 2×10^3 , the fluxes increase linearly with Ra_T and is nearly independent of Ra_S when temperature Rayleigh number exceeds 100. As a result, the fluxes change remarkably only when concentration Rayleigh number is small and temperature Rayleigh number is large compared with RDC without a temperature gradient. In other words, the flux increment is highly related to the density ratio. After rescaling concentration flux with the effective Rayleigh number Ra_e in figure 9, we find that it decreases with density ratio and asymptotically attains a constant value. This asymptote will be explained by the scale analysis in the following section.

3.2.2. Scale analysis for concentration-dominant and temperature-dominant flow

Examine two contrasting scenarios with both high- Ra_S and Ra_T characterised by the density ratio, with one corresponding to the concentration-dominant regime where $\Lambda \ll 1$ and the other to the temperature-dominant regime with $\Lambda \gg 1$. In the former case, the dominant driving forces for the flow are concentration, while in the latter, temperature takes precedence.

The concentration-dominant flow in the boundary layers is featured by the horizontal and vertical length scales as $x(\text{or } y) \sim H$ and $z \sim \delta_S$, respectively. The scales of the velocity are (U, V, W) . The scale equivalences recommended by the governing equations are

$$\frac{U}{H} \sim \frac{W}{\delta_S}, \quad W \sim \frac{Kg\Delta\rho_S^*}{\mu}, \quad U \frac{\Delta T^*}{H} \sim \kappa_T \frac{\Delta T^*}{\delta_T^2}, \quad W \frac{\Delta S^*}{\delta_S} \sim \phi \kappa_S \frac{\Delta S^*}{\delta_S^2}. \quad (3.6a-d)$$

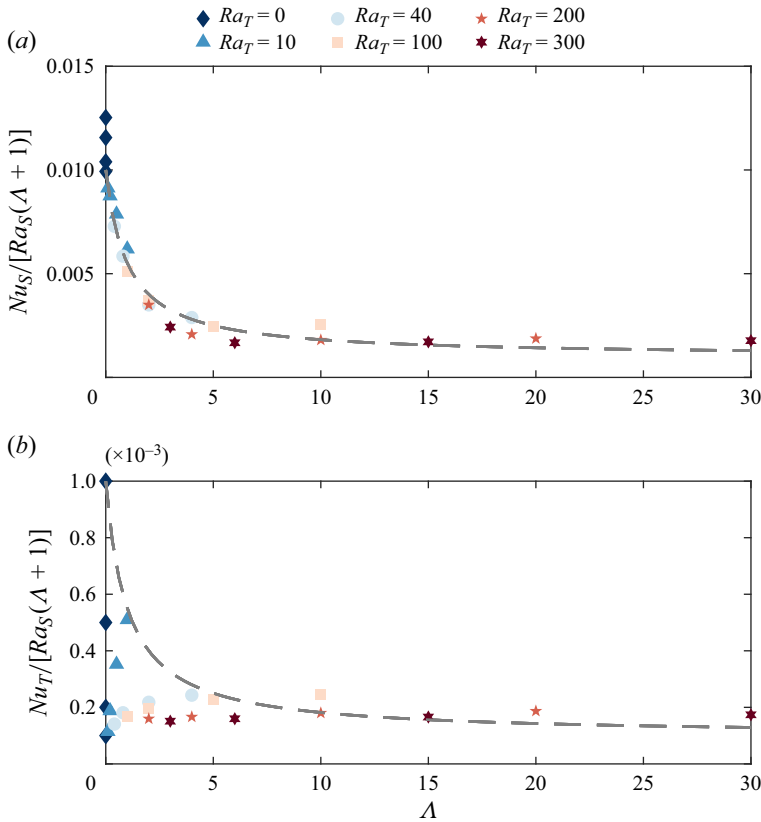


Figure 9. The variation of (a) concentration and (b) heat flux rescaled by the effective Rayleigh number with density ratio. The grey dashed lines are (3.6a–d) given by scale analysis.

The above equivalences can yield

$$Nu_{S1} \sim \frac{\delta_S}{H} \sim Ra_S, \quad Nu_{T1} \sim \frac{\delta_T}{H} \sim Ra_S Le^{-1/2}. \quad (3.7a,b)$$

Similarly, the scale equivalences for temperature-dominant flow are

$$\frac{U}{H} \sim \frac{W}{\delta_T}, \quad W \sim \frac{Kg\Delta\rho_T^*}{\mu}, \quad U \frac{\Delta T^*}{H} \sim \kappa_T \frac{\Delta T^*}{\delta_T^2}, \quad \frac{\delta_S}{\delta_T} W \frac{\Delta S^*}{\delta_S} \sim \phi \kappa_S \frac{\Delta S^*}{\delta_S^2}. \quad (3.8a-d)$$

The above equivalences can yield

$$Nu_{S2} \sim Ra_T Le^{1/2}, \quad Nu_{T2} \sim Ra_T. \quad (3.9a,b)$$

A straightforward assumption of the concentration and heat flux in a flow driven by both concentration and temperature gradients is that $Nu_S = \alpha_0(Ra_S + Ra_T Le^{1/2})$ and $Nu_T = \alpha_0(Ra_S Le^{-1/2} + Ra_T)$, which can be alternatively written as

$$\frac{Nu_S}{Ra_e} = \frac{(1 - Le^{-1/2})\alpha_0}{\Lambda + 1} + Le^{-1/2}\alpha_0, \quad \frac{Nu_T}{Ra_e} = \frac{(Le^{-1/2} - Le^{-1})\alpha_0}{\Lambda + 1} + Le^{-1}\alpha_0. \quad (3.10a,b)$$

Using the aforementioned $\alpha_0 \approx 0.01$ and the fixed $Le = 100$, then the above relation can be simplified to

$$\frac{Nu_S}{Ra_e} = \frac{0.009}{\Lambda + 1} + 0.001, \quad \frac{Nu_T}{Ra_e} = \frac{0.0009}{\Lambda + 1} + 0.0001. \quad (3.11a,b)$$

The above relations are also depicted in [figure 9](#). The numerical measurements for concentration flux are in good agreement with the relation derived from scale analysis for all density ratios we have explored. However, the correlation for Nu_T displays a significant discrepancy, particularly at low density ratios, roughly $\Lambda < 5$, and mostly at $Ra_T < 100$. This disparity arises because the linear scaling of flux and Rayleigh number is more precise at high- Ra conditions, typically exceeding 10^3 , for single-component RDC ([Hewitt et al. 2014](#)). The parameter space of Ra_T investigated in this study does not fall within the high- Ra range. Consequently, the heat flux measurements deviate from the scaling analysis relation at low density ratios.

3.3. Influence of domain size

To minimise the influence of horizontally periodic boundary conditions, the computational domain must be chosen carefully to ensure the presence of sufficient convective cells. To investigate the effect of domain size, we conduct a series of simulations at fixed Rayleigh numbers, $Ra_S = 10^4$ and $Ra_T = 100$, with six different aspect ratios $\mathcal{R} = 1/8, 1/4, 1/2, 1, 2$ and 4 . The aspect ratio is defined as the ratio of domain width in the x direction to height in the z direction. The simulation details are summarised in [table 2](#) in [Appendix A](#). Horizontal slices of concentration near the top boundary at $z = 0.99$ are shown in [figure 10\(a–f\)](#) with increasing \mathcal{R} . The narrow width in the x direction significantly affects flow structures. For small aspect ratios, the flow is confined in the x direction, leading to strips parallel to x direction because of horizontal periodicity (see [figure 10a,b](#)). As the aspect ratio increases, flow structures evolve into more complex formations and convective cells are more visible. We also analyse the mean radial wavenumber for concentration at $z = 0.9$ to examine its variation with \mathcal{R} in [figure 10\(g\)](#). Here k_{rS} decreases with increasing \mathcal{R} and remains almost constant for $\mathcal{R} \geq 1$. Considering the variations in flow structures and k_{rS} , we employ a computational domain of size $4H \times 4H \times H$ for all simulations. It is reasonable to conclude that this domain size is sufficient to capture the flow structures.

4. Heterogeneous porous media

The permeability field is generated as described in the previous section. Here, two typical examples with different correlation lengths and the same Dykstra–Parsons coefficient are presented in [figure 11](#). The spatial distribution of permeability is distinct. The increase of l_r results in two effects on the distribution of permeability. On the one hand, the region of relatively larger permeability (darker region in [figure 11](#)) is more concentrated over a wide area. On the other hand, the maximum value of permeability becomes smaller. In our simulations, the ratio of maximum and minimum of generated permeability can reach $\mathcal{O}(10^3)$, which limits the explored Rayleigh number to a moderate value, i.e. $Ra_S = 10^3$, in the context of permeability heterogeneity due to computational cost.

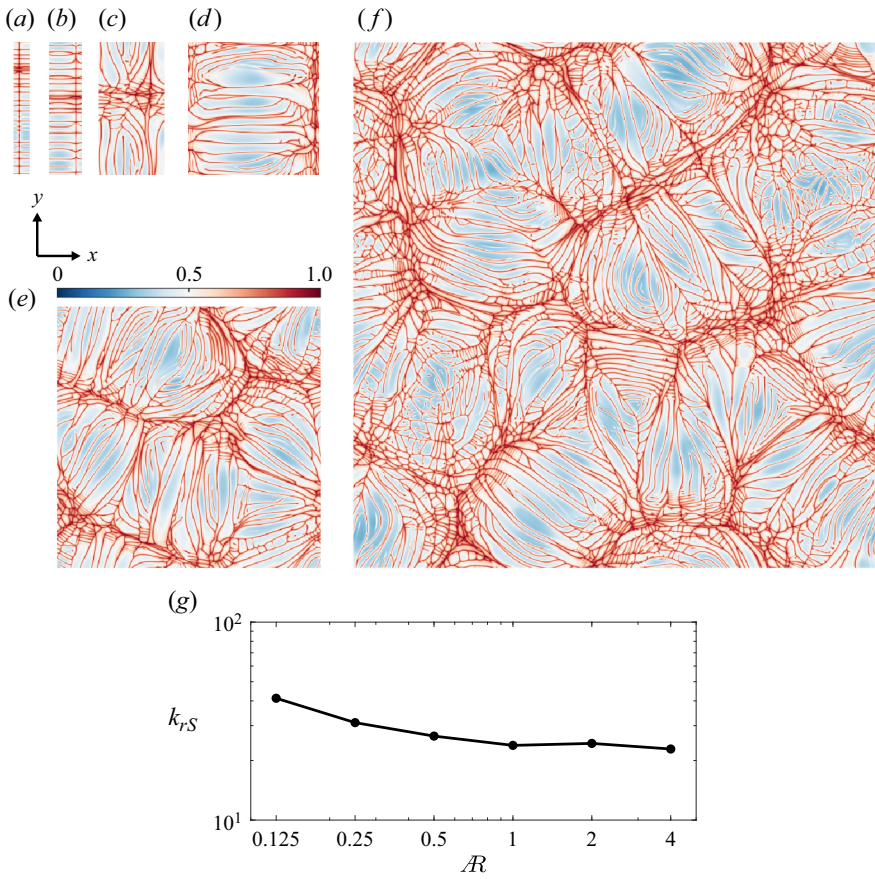


Figure 10. Influence of domain width at different aspect ratios \mathcal{R} . Horizontal slices of concentration near the top boundary at $z = 0.99$ are presented in (a–f) corresponding to $\mathcal{R} = 1/8, 1/4, 1/2, 1, 2$ and 4 , respectively. The mean radial wavenumber for concentration slices at $z = 0.9$ is presented in (g).

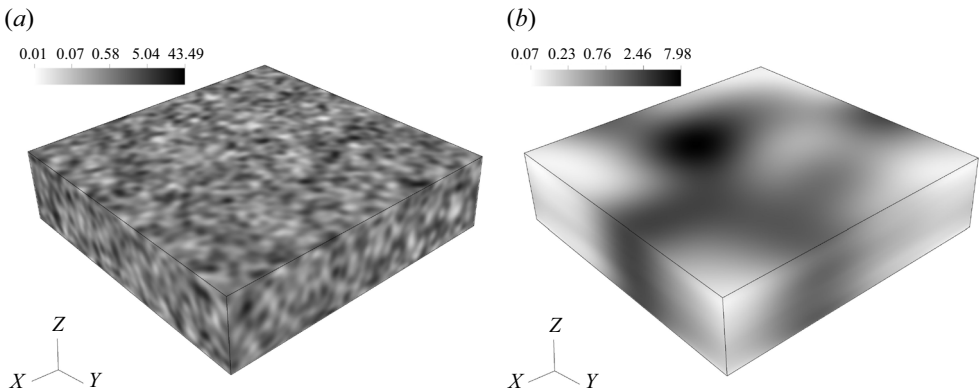


Figure 11. Examples of generated permeability field f with $V_{DP} = 0.6$: (a) $l_r = 0.1$; (b) $l_r = 1.0$.

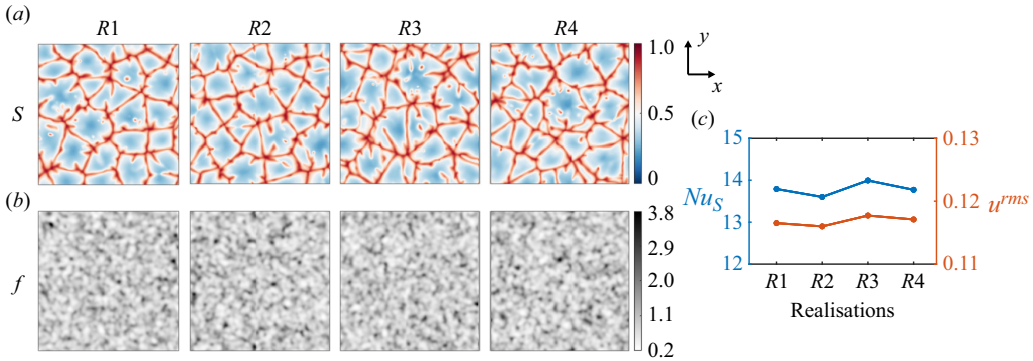


Figure 12. Four realisations of permeability field with $l_r = 0.1$, $V_{DP} = 0.3$ are generated and marked as R1 to R4. Flow structures and statistical results of these realisations at Rayleigh numbers $Ra_S = 10^3$, $Ra_T = 0$ are presented. (a,b) Horizontal slices of concentration and normalised permeability at $z = 0.9$, respectively. (c) Variations of Nusselt number and r.m.s. velocity with realisations.

4.1. Validation for various realisations

In this study, the permeability fields are generated by a statistical random Gaussian field. It is necessary to prove that the numerical results are independent of realisations. To validate such an independence, we generate four realisations of permeability field under the same set of parameters with $l_r = 0.1$ and $V_{DP} = 0.3$. Numerical simulations have been conducted at Rayleigh numbers $Ra_S = 10^3$, $Ra_T = 0$ for these realisations. Simulation details are provided in Appendix A. Figure 12(a,b) show horizontal slices of concentration and the normalised permeability field at $z = 0.9$, which exhibits similar structures regardless of realisations. The statistical concentration Nusselt number and r.m.s. velocity in figure 12(c) remain almost constant values for the four realisations. The maximum relative error, defined as the absolute error between the measurements and the mean value, divided by the mean value itself, is 1.48 % for Nu_S and 0.76 % for u^{rms} . Therefore, it is reasonable to conclude that our results are independent of realisations of the permeability field.

4.2. Single-component convection at $Ra_S = 10^3$

First, we consider convection solely driven by concentration at a fixed Rayleigh number $Ra_S = 10^3$. By varying l_r from 0.1 to 1.0, and V_{DP} from 0.1 to 0.6, the flow patterns and global responses vary accordingly. It is anticipated that higher permeability values are prone to manifest as heterogeneity strengthens. Meanwhile, the flow tends to preferentially traverse regions with greater permeability, where the resistance is weaker. As a result, the flow becomes more concentrated, and the velocity magnitude amplifies notably at these preferential locations.

Flow structures in our simulations shown in figure 13 are consistent with the above inferences. It is notable that velocity and concentration structures are largely influenced by both correlation length and heterogeneity intensity. When $l_r = 0.1$ (see the left three columns of figure 13), i.e. for a small correlation length, large values of permeability are confined in small spots with diameter equivalent to l_r . If the porous medium is homogeneous, the concentration slice near the top boundary comprises hexagonal cells with distinct boundary lines. This pattern persists when V_{DP} is small. However, as V_{DP} increases, those boundary lines disperse horizontally and become coarser. The hexagonal

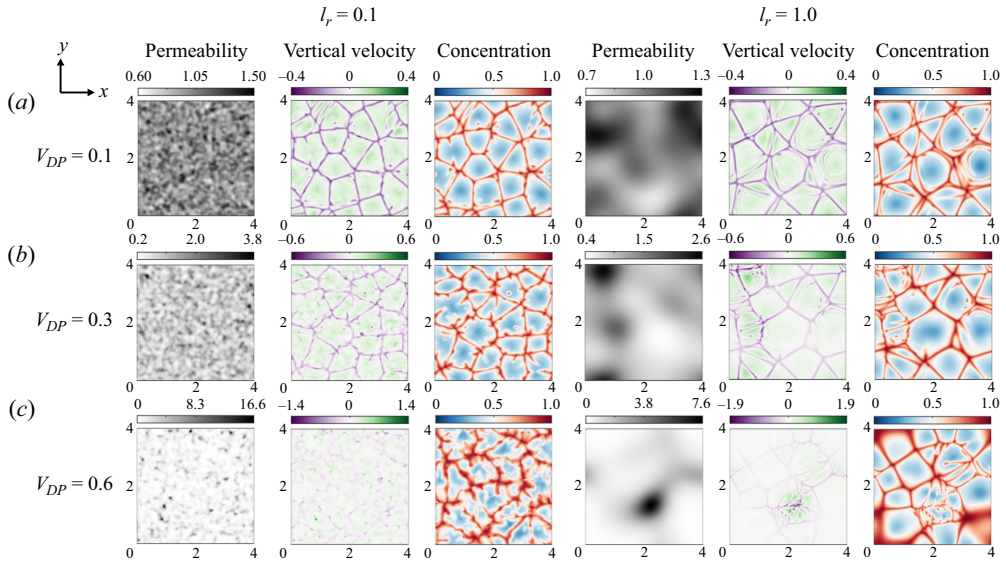


Figure 13. Horizontal slices of permeability, vertical velocity and concentration at $z = 0.9$. The left three columns correspond to $l_r = 0.1$, and the right three columns to $l_r = 1.0$. Each row represents a Dykstra–Parsons coefficient, ranging from (a) 0.1 to (c) 0.6. The Rayleigh numbers are $Ra_S = 10^3$ and $Ra_T = 0$ for all simulations.

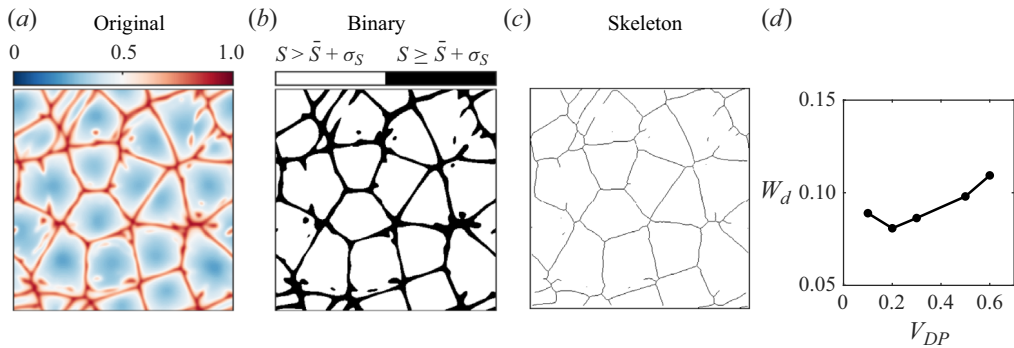


Figure 14. In (a–c) the controlling parameters are set at $Ra_S = 10^3$, $Ra_T = 0$, $l_r = 0.1$ and $V_{DP} = 0.1$. (a) Horizontal slices of concentration at $z = 0.9$. (b) Binary contour of (a) with dark region indicating $S \geq \bar{S} + \sigma_S$. (c) Skeleton of (b) extracted by the Matlab *bwskel* function. (d) Variation of structure width with V_{DP} at $Ra_S = 10^3$, $Ra_T = 0$ and $l_r = 0.1$.

convection cells are difficult to recognise when $V_{DP} = 0.6$. Such coarseness indicates the intensified horizontal dispersion as heterogeneity strengthens for small l_r . To quantitatively describe this effect, we identify the boundaries of convection cells with regions where $S \geq \bar{S} + \sigma_S$ in the horizontal slice of concentration. This allows us to generate a binary field as shown in figure 14(b). Utilising the Matlab *bwskel* function, we extract the skeleton of above binary field in figure 14(c). By dividing the area of dark region in the binary field by the length of skeleton, we define a characteristic structure width W_d to as a measure of horizontal dispersion effect for small correlation length. Its variation with V_{DP} in figure 14(d) shows that the structure width generally increases with heterogeneity levels, except for one point $V_{DP} = 0.1$ at the very beginning.

Double-diffusive convection

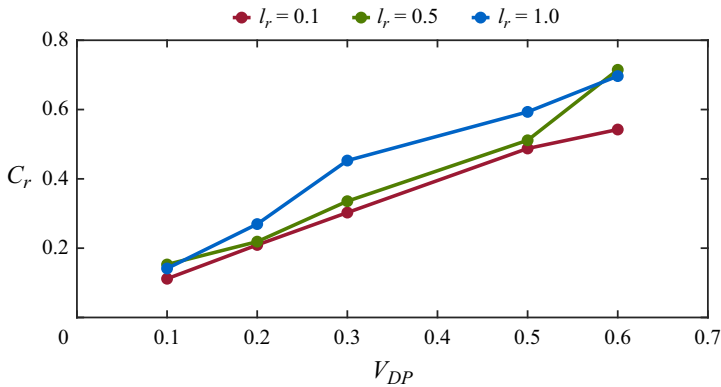


Figure 15. The variation of correlation coefficient C_r with V_{DP} .

When $l_r = 1.0$ (see the right three columns of [figure 13](#)), the correlation length is larger than the typical size of convection cells in RDC in homogeneous porous media. The flow patterns are different from simulations with small l_r . Increasing V_{DP} leads to the merger and reorganisation of convection cells, resulting in a coexistence of both large cells and small structures. Furthermore, the residence of small structures corresponds to regions with large permeability. This phenomenon is contributed to by the fact that the local Rayleigh number is proportional to permeability and comparably large over a wide range (larger than the given overall $Ra_S = 10^3$), thus triggering more vigorous convection locally. Previous investigations ([Hewitt *et al.* 2014](#); [Pirozzoli *et al.* 2021](#); [De Paoli *et al.* 2022](#)) into convection in porous media have revealed that convection scales become smaller as Rayleigh numbers increase. Hence, smaller structures emerge when V_{DP} is large, owing to intensified convective motions occurring at locations characterised by higher permeability. This intensification also extends to the vertical velocity in these regions.

To provide a quantitative description of how permeability influences the velocity field, the correlation coefficient C_r of permeability and magnitude of vertical velocity is calculated and presented in [figure 15](#). The coefficient demonstrates a linear increase with heterogeneity and is largely unaffected by the specified correlation lengths. As the porous media exhibit greater heterogeneity, the correlation between permeability and the magnitude of vertical velocity strengthens, which is consistent with our expectations.

[Figure 16\(a\)](#) shows the variation of u^{rms} with correlation length l_r . When the heterogeneity is relatively weak, saying $V_{DP} = 0.1 \sim 0.3$, u^{rms} is nearly unchanged and close to that of the homogeneous simulation. Only when V_{DP} is large does u^{rms} remarkably deviate from homogeneous value. Yet it does not largely vary with the correlation length. For comparison, in [figure 16\(b\)](#), it is clear that u^{rms} monotonically increases with V_{DP} , which is consistent with the fact that maximum permeability increases with V_{DP} . The three coloured lines roughly collapse, suggesting that the correlation length has minor effect on u^{rms} compared with the strength of heterogeneity. In other words, the statistical velocity remains nearly unchanged regardless of how the permeability field with the same level of heterogeneity is spatially distributed.

Another important global response is the concentration flux at the upper and lower walls characterised by Nusselt number. In [figure 17\(a\)](#), Nu_S shows non-monotonic variations with increasing heterogeneity for a fixed correlation length. For $l_r = 0.1$, the flux is always larger than that of the homogeneous case and reaches the maximum at a

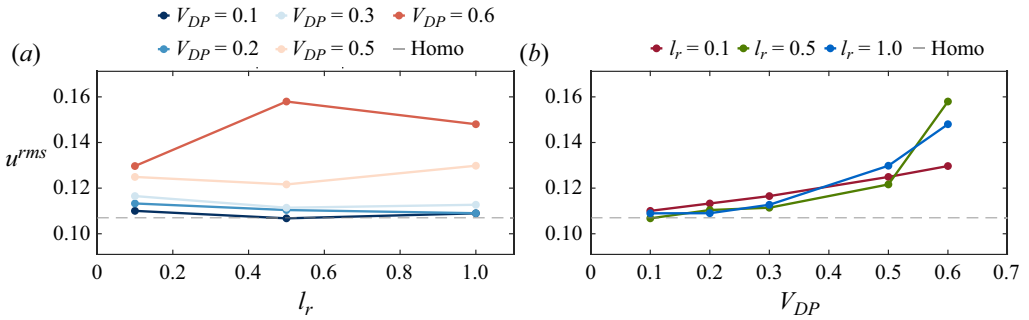


Figure 16. The variations of r.m.s. of velocity u^{rms} with (a) correlation length l_r and (b) Dykstra–Parsons coefficient V_{DP} . The Rayleigh numbers are $Ra_S = 10^3$ and $Ra_T = 0$ for all simulations. The grey dashed line represents the corresponding value in homogeneous porous media under the same Rayleigh number.

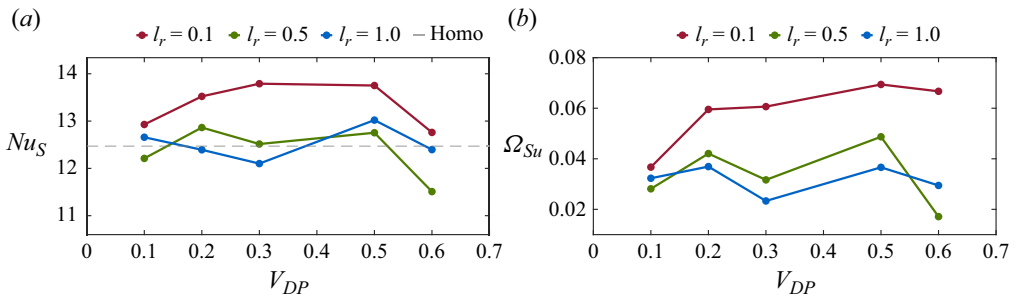


Figure 17. The variations of (a) concentration flux Nu_S and (b) portion of area Ω_{Su} containing both high concentration and downward velocity at $z = 0.1$ with Dykstra–Parsons coefficient V_{DP} . The Rayleigh numbers are $Ra_S = 10^3$ and $Ra_T = 0$ for all simulations.

moderate heterogeneity. For the other two l_r , the flux fluctuates around the homogeneous value as V_{DP} increases. The Nu_S decreases from a relatively large value from $V_{DP} = 0.5$ to $V_{DP} = 0.6$ compared with other V_{DP} on the green curve. The relative variation, defined as the absolute error between current Nu_S and Nu_S in homogeneous convection divided by the homogeneous value, is 7.7% at $V_{DP} = 0.6$. Although we are not able to disentangle the different variations between three explored l_r , the non-monotonic behaviour observed can be attributed to the ability of the flow to transport high concentration from top to bottom, which is quantified by the portion of area Ω_{Su} containing both high concentration and downward velocity. Specifically, we calculate the total area in the $z = 0.1$ plane satisfying $S' > S^{std}$ and $u'_z < -u'_z{}^{std}$, and then divide it by the area of the plane. Here, S' and u'_z are the deviations from the horizontally averaged concentration and vertical velocity, respectively, and S^{std} and $u'_z{}^{std}$ are the corresponding standard deviations. The variations of Ω_{Su} in figure 17(b) also exhibit non-monotonic behaviour, aligning with the trends of Nu_S in figure 17(a).

4.3. DDC at $Ra_S = 10^3$, $Ra_T = 50$

In the last subsection, the driving force only consists of concentration difference. In this subsection, an additional driving force stemming from an aiding temperature difference is introduced, maintaining a fixed temperature Rayleigh number of $Ra_T = 50$. The parameter

Double-diffusive convection

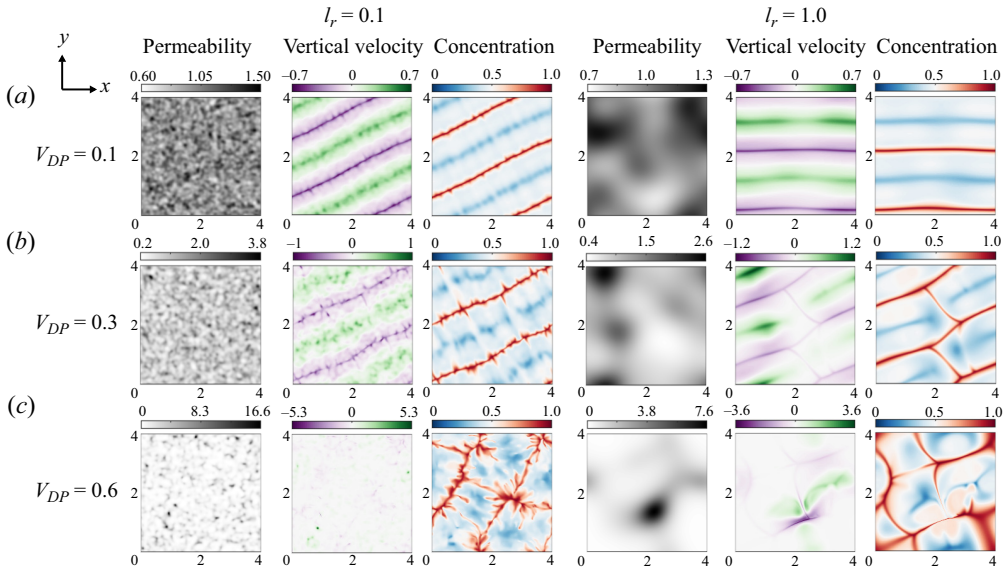


Figure 18. Horizontal slices of permeability, vertical velocity and concentration at $z = 0.9$. The left three columns correspond to $l_r = 0.1$, and the right three columns to $l_r = 1.0$. The Rayleigh numbers are $Ra_S = 10^3$ and $Ra_T = 50$ for all simulations.

l_r varies from 0.1 to 1.0, and V_{DP} ranges from 0.1 to 0.6. The permeability field for each l_r and V_{DP} remains the same as the previous subsection.

From our earlier discussion on DDC in homogeneous porous media, we know that for the specified driving forces of $Ra_S = 10^3$ and $Ra_T = 50$, the predominant flow structures manifest as vertically parallel sheet-like formations. In figure 18, we present typical structures of vertical velocity and concentration considering permeability heterogeneity. Compared with those in the absence of a temperature Rayleigh number, we observe similar variations for different V_{DP} values at a fixed l_r . Specifically, when l_r is small (see the left three columns of figure 18), horizontal dispersion and coarseness of sheet-like concentration structures are noticeable. The parallel characteristic of flow structures seems to vanish as heterogeneity becomes strong. When l_r is large (see the right three columns of figure 18), parallel sheets begin to interconnect and interact with each other with increasing V_{DP} . In addition, flow velocities are more pronounced in regions characterised by higher permeability.

In contrast to the non-monotonic variations observed in the concentration flux Nu_S for single-component convection in heterogeneous porous media, the flux Nu_S exhibits a consistent decrease with increasing V_{DP} across all three correlation lengths, as shown in figure 19(a) for DDC. Furthermore, the flux considering permeability heterogeneity is generally lower than that of homogeneous convection under the same driving forces. Similar to the analysis in the absence of Ra_T , we calculate the portion of area with high concentration and downward velocity. The decreasing behaviour of Nu_S is well captured by the decreasing Ω_{Su} in figure 19(b), indicating that the flow becomes less effective at transporting concentration from top to bottom with greater heterogeneity, regardless of the correlation lengths.

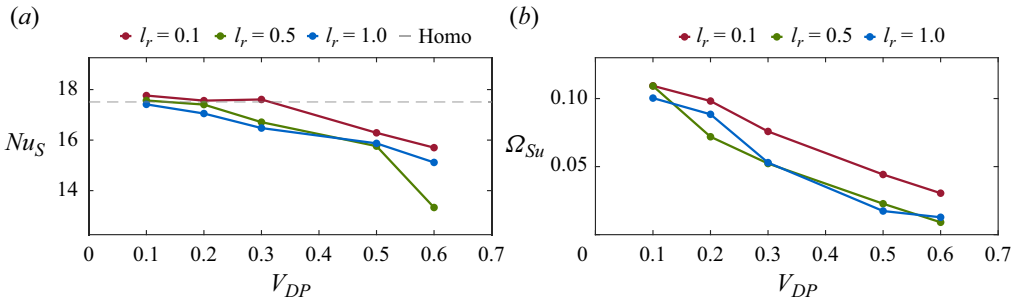


Figure 19. The variations of (a) concentration flux Nu_S and (b) portion of area Ω_{Su} containing both high concentration and downward velocity at $z = 0.1$ with Dykstra–Parsons coefficient V_{DP} . The Rayleigh numbers are $Ra_S = 10^3$ and $Ra_T = 50$ for all simulations.

4.4. Qualitative comparisons with previous findings

Previous studies on permeability heterogeneity have primarily focused on the convective dissolution process, or the above-mentioned one-sided convection. While direct comparisons between their results and ours are not feasible due to different boundary conditions at the bottom, we can analyse the influences of various control parameters and gain valuable insights.

Specifically, Ranganathan *et al.* (2012) and Farajzadeh *et al.* (2010) investigated single-component convective dissolution in heterogeneous porous media, where a no-flux condition for concentration is employed on the bottom boundary. Our findings are consistent with their observations in that the correlation length has a minor effect on the dissolution rate (concentration flux in our study) compared with the heterogeneity level. In addition, flow pattern regimes differ at various correlation lengths and heterogeneity levels. For instance, the flow structures at small V_{DP} are similar to those in the homogeneous case, while at large V_{DP} and small l_r , the flow is more dispersive. However, we also noted some differences in the variations of the dissolution rate (concentration flux in our study) with heterogeneity levels, which we attribute to different boundary conditions for concentration at the bottom, resulting in a time-evolving transient process in their studies and a statistically steady state in ours. In addition, the coexistence of both large and small structures at large l_r and V_{DP} is not observed in their studies. This difference can be attributed to the dimensional differences between their 2-D simulations and our 3-D simulations.

Islam *et al.* (2014b) studied convective dissolution with geothermal gradients in reservoirs with permeability variations. They found that CO_2 dissolution is enhanced with increasing both Ra_S and V_{DP} , which differs from the variations of Nu_S in our study. They also concluded that the geothermal effect has a minor effect on the overall dissolution process, which seems contradictory to our results. However, a detailed examination of their parameters reveals consistent results regarding the effect of the geothermal gradient, with the concentration Rayleigh number of $10^2 \leq Ra_S \leq 10^4$, the buoyancy ratio of $2 \leq N \leq 100$, and a fixed Lewis number of 310. The definition of N is $N = \beta_c \Delta c / \beta_T \Delta T = Ra_S / (Le Ra_T)$, which is exactly the reciprocal of the density ratio Λ in our study. In other words, their density ratio ranges from $0.01 \leq \Lambda \leq 0.5$. Using the relation $\Lambda = Le Ra_T / Ra_S$, the temperature Rayleigh number ranges from $0.0032 \lesssim Ra_T \lesssim 16.13$. Our results, as well as those in Hu *et al.* (2023), show that within these ranges of density ratio and temperature Rayleigh number, the geothermal gradient has a minor effect on dissolution.

5. Conclusion

In conclusion, we have investigated 3-D DDC in homogeneous and heterogeneous porous media by direct numerical simulations. The temperature and concentration gradients are set to be gravitationally unstable, with the fluid being cold saturated at the top boundary and warm fresh at the bottom. The Lewis number and heat capacity ratio are fixed at 100 and 1, respectively, in our simulations.

For homogeneous porous media, the concentration Rayleigh number Ra_S ranges from 10^3 to 10^4 , and the temperature Rayleigh number Ra_T ranges from 0 to 300. Numerical measurements of r.m.s. velocity exhibits linear scaling with the density ratio defined as $\Lambda = Ra_T Le / Ra_S$. The linearity is related to the fact that the total driving forces of convection originate from density differences by both temperature and concentration differences. A theoretical relation between the r.m.s. velocity, concentration Rayleigh numbers, and Nusselt numbers is obtained by a volumed average of the governing equations. The numerical measurements show excellent agreement with the theoretical predictions. For a fixed Ra_S , the flow structures show significant changes when Ra_T exceeds Ra_{cr} compared with single-component convection. The temperature field mainly consists of large-scale structures, which interact with concentration finger structures at a relatively smaller scale. Flow patterns alter from sheet-like structures to cellular structures as Ra_T increases. The density ratio also influences flow structures. The size of dominant structures is typically quantified by the mean radial wavenumber k_{rS} at the centre plane $z = 0.5$. By defining an effective Rayleigh number as $Ra_e = Ra_S + Le Ra_T$, the mean radial wavenumber roughly scales as $k_{rS} \approx 0.23 Ra_e^{0.47}$. Although this scale is a loose power fit of the measurements, it can capture the trend of variations. By analysing the mean profiles of concentration, a negative concentration gradient in the bulk region is observed when Ra_T is larger than 40, which is opposite to the imposed concentration gradient on the boundaries. The non-dimensionalised fluxes are measured as the mean value on two boundaries. The concentration flux Nu_S increases with increasing Ra_S for a fixed Ra_T . Utilising the scale analysis, we obtain unified predictions for both Nu_S and Nu_T by assuming a linear relation. The prediction of Nu_S agrees well with numerical measurements, while Nu_T deviates from its prediction when Λ is roughly less than 5. The influence of domain size is also included. Results reveal that our size of computational domain $4H \times 4H \times H$ is sufficient to capture the flow structures and can provide reliable statistics.

For heterogeneous porous media, the concentration Rayleigh number is fixed at $Ra_S = 10^3$. The permeability field is generated at various Dykstra–Parsons coefficients V_{DP} and correlation lengths l_r using a random Gaussian field. Here V_{DP} ranges from 0.1 to 0.6, and l_r ranges from 0.1 to 1. Validation for various realisations with $l_r = 0.1$ and $V_{DP} = 0.3$ shows that our results are independent of permeability realisations. Both single-component convection ($Ra_T = 0$) and DDC ($Ra_T = 50$) are considered. It is expected that the flow travels more rapidly at locations with larger permeability, where the resistance is smaller. When $Ra_T = 0$, the cellular structures in homogeneous porous media coarsen as heterogeneity strengthens for small correlation length $l_r = 0.1$. The typical width of flow structures generally increases with increasing heterogeneity levels except for $V_{DP} = 0.1$. However, if correlation length $l_r = 1$ is larger than typical size of convective cells in homogeneous porous media at the same Ra_S , the concentration structures consist of both large cells and small structures for $V_{DP} = 0.6$. Variations of r.m.s. velocity and concentration flux indicate that correlation length has a minor effect compared with V_{DP} . When $Ra_T = 50$, parallel sheet structures are dominant in the absence of heterogeneity. For small l_r , increasing V_{DP} also results in the coarseness of sheet structures, which alters largely when $V_{DP} = 0.6$. For large l_r , parallel sheets begin to interconnect at a

moderate heterogeneity $V_{DP} = 0.3$. The concentration flux displays a decreasing tendency with increasing heterogeneity regardless of correlation lengths. The variations in the concentration flux are related to the flow's ability to transport high concentration from top to bottom, which is quantified by the portion of area containing both high concentration and downward velocity. Finally, we have compared our results with previous findings from the literature.

Overall, our study provides insights into the role of unstable geothermal gradients in canonical two-sided RDC, considering both homogeneous and heterogeneous porous media. From the perspective of convection, geothermal gradients should indeed be considered and have significant influences on the mass transfer in porous media systems.

Funding. This work is financially supported by Laoshan Laboratory under grant no. LSKJ202202000.

Declaration of interest. The authors report no conflict of interest.

Author ORCIDs.

Chenglong Hu <https://orcid.org/0000-0002-2935-9258>;

Yantao Yang <https://orcid.org/0000-0001-5065-2769>.

Appendix A. Summary of numerical details

The simulation details of DDC in homogeneous porous media are listed in [table 1](#) with fixed Lewis number $Le = 100$ and heat capacity ratio $\sigma = 1$. Details to explore influence of domain size are listed in [table 2](#) with fixed Rayleigh numbers $Ra_S = 10^4$, $Ra_T = 100$. Details to validate that results are independent of permeability realisations are listed in [table 3](#). Details of convection in heterogeneous porous media are listed in [table 4](#) for single-component convection and [table 5](#) for DDC, respectively.

Appendix B. Details of exact relation for Pe

Similar to the analysis in Zhu *et al.* (2024), a theoretical relation for Pe , the Nusselt and Rayleigh numbers are presented in this appendix. An alternative definition of Nusselt numbers is

$$Nu_T = \frac{Ra_S}{Le} \langle u_z T \rangle_A - \left\langle \frac{\partial T}{\partial z} \right\rangle_A, \quad Nu_S = -Ra_S \langle u_z S \rangle_A + \left\langle \frac{\partial S}{\partial z} \right\rangle_A. \quad (B1a,b)$$

Here $\langle \cdot \rangle_A$ denotes an average over time and a horizontal surface A . By taking the dot product of \mathbf{u} with both sides of (2.3b) and combining it with the incompressible continuity (2.3a), we obtain

$$|\mathbf{u}|^2 = -\nabla \cdot (p\mathbf{u}) + (\Lambda T - S)u_z. \quad (B2)$$

The time and volume average (indicating by $\langle \cdot \rangle$) reads

$$\langle |\mathbf{u}|^2 \rangle = -\frac{1}{L^2} \iint_{\partial S} (p\mathbf{u}) \cdot \hat{\mathbf{n}} \, dS + \Lambda \langle Tu_z \rangle - \langle Su_z \rangle, \quad (B3)$$

where L is the dimensionless aspect ratio, ∂S is the boundary surface of the domain and $\hat{\mathbf{n}}$ is the normal unit vector for the surface elements. The first term on the right-hand side of

Double-diffusive convection

Ra_S	Ra_T	Λ	L/H	$N_x(m_x)$	$N_y(m_y)$	$N_z(m_z)$	N_t	Nu_S	Nu_T	u^{rms}
$Ra_S = 10^3$	0	0	4	384(1)	384(1)	96(1)	100	12.53	1.00	0.11
	10	1	4	384(1)	384(1)	96(1)	100	12.38	1.02	0.12
	40	4	4	384(1)	384(1)	96(1)	100	14.43	1.22	0.32
	100	10	4	384(1)	384(1)	192(1)	100	27.84	2.69	1.31
	200	20	4	384(1)	384(1)	192(1)	100	39.41	3.93	2.43
	300	30	4	576(2)	576(2)	192(2)	5	54.92	5.38	3.63
$Ra_S = 2 \times 10^3$	0	0	4	768(1)	768(1)	144(1)	80	23.12	1.00	0.11
	10	0.5	4	768(1)	768(1)	144(1)	80	23.61	1.06	0.11
	40	2	4	768(1)	768(1)	144(1)	80	20.97	1.31	0.20
	100	5	4	768(1)	768(1)	192(1)	80	29.64	2.73	0.67
	200	10	4	768(1)	768(1)	192(1)	80	39.71	3.96	1.23
	300	15	4	768(1)	768(1)	288(1)	80	54.82	5.30	1.80
$Ra_S = 5 \times 10^3$	0	0	4	1152(1)	1152(1)	192(1)	40	51.96	1.00	0.10
	10	0.2	4	1152(1)	1152(1)	192(1)	40	52.49	1.13	0.10
	40	0.8	4	1152(1)	1152(1)	288(1)	40	52.60	1.63	0.14
	100	2	4	1536(1)	1536(1)	288(1)	20	55.85	2.94	0.30
	200	4	4	1536(1)	1536(1)	288(1)	20	51.95	4.16	0.51
	300	6	4	1536(1)	1536(1)	288(1)	20	58.50	5.59	0.75
$Ra_S = 10^4$	0	0	4	2304(1)	2304(1)	288(1)	10	99.30	1.00	0.10
	10	0.1	4	2304(1)	2304(1)	288(1)	10	100.44	1.26	0.10
	40	0.4	4	2304(1)	2304(1)	288(1)	10	102.00	1.97	0.12
	100	1	4	2304(1)	2304(1)	384(1)	10	101.72	3.36	0.18
	200	2	4	2304(1)	2304(1)	576(1)	10	104.99	4.79	0.29
	300	3	4	2304(1)	2304(1)	576(1)	10	97.01	6.04	0.40

Table 1. Summary of simulations for DDC in homogeneous porous media. Columns from left to right are the concentration Rayleigh number, temperature Rayleigh number, density ratio, aspect ratio, resolutions in the x -axis, y -axis, z -axis (with refinement factors for multiple resolutions), non-dimensionalised simulating time, averaged concentration flux, heat flux and r.m.s. velocity, respectively.

Ra_S	Ra_T	Λ	$L_x/H \times L_y/H$	$N_x(m_x)$	$N_y(m_y)$	$N_z(m_z)$	N_t	Nu_S	Nu_T	u^{rms}
10^4	100	1	$1/8 \times 1$	96(1)	768(1)	384(1)	80	105.89	3.11	0.18
			$1/4 \times 1$	192(1)	768(1)	384(1)	80	102.11	2.86	0.17
			$1/2 \times 1$	384(1)	768(1)	384(1)	80	98.40	3.04	0.17
			1×1	768(1)	768(1)	384(1)	40	94.62	3.13	0.18
			2×2	1152(1)	1152(1)	384(1)	20	99.92	3.13	0.18
			4×4	2304(1)	2304(1)	384(1)	10	101.72	3.36	0.18

Table 2. Summary of simulations to explore the influence of domain size in DDC in homogeneous porous media. The Rayleigh numbers are fixed at $Ra_S = 10^4$ and $Ra_T = 100$. Columns from left to right are the concentration Rayleigh number, temperature Rayleigh number, density ratio, aspect ratio, resolutions in the x -axis, y -axis, z -axis (with refinement factors for multiple resolutions), non-dimensionalised simulating time, averaged concentration flux, heat flux and r.m.s. velocity, respectively.

(B3) vanishes due to the non-penetration boundary condition:

$$\frac{1}{L^2} \iint_{\partial S} (p\mathbf{u}) \cdot \hat{\mathbf{n}} \, dS = -\frac{1}{L^2} \iint_{\partial S(z=0)} pu_z \, dS + \frac{1}{L^2} \iint_{\partial S(z=1)} pu_z \, dS = 0. \quad (\text{B4})$$

l_r	V_{DP}	L	$N_x(m_x)$	$N_y(m_y)$	$N_z(m_z)$	N_t	Nu_S	u^{rms}
0.1	0.3	4	576(1)	576(1)	192(1)	40	13.79	0.117
							13.60	0.116
							13.99	0.118
							13.77	0.117

Table 3. Summary of simulations for single-component convection at $Ra_S = 10^3$, $Ra_T = 0$ in heterogeneous porous media for the validation of realisations. Columns from left to right are the correlation length, Dykstra–Parsons coefficient, aspect ratio, resolutions in the x -axis, y -axis, z -axis (with refinement factors for multiple resolutions), non-dimensionalised simulating time, averaged concentration flux and r.m.s. velocity, respectively.

l_r	V_{DP}	L	$N_x(m_x)$	$N_y(m_y)$	$N_z(m_z)$	N_t	Nu_S	u^{rms}
0.1	0.1	4	384(1)	384(1)	192(1)	60	12.93	0.110
							13.52	0.113
							13.79	0.117
							13.75	0.125
							12.76	0.130
0.5	0.1	4	384(1)	384(1)	192(1)	60	12.21	0.107
							12.86	0.110
							12.52	0.111
							12.75	0.122
							11.51	0.158
1	0.1	4	384(1)	384(1)	192(1)	60	12.66	0.109
							12.39	0.109
							12.10	0.113
							13.02	0.130
							12.40	0.148

Table 4. Summary of simulations for single-component convection at $Ra_S = 10^3$ in heterogeneous porous media. Columns from left to right are the correlation length, Dykstra–Parsons coefficient, aspect ratio, resolutions in the x -axis, y -axis, z -axis (with refinement factors for multiple resolutions), non-dimensionalised simulating time, averaged concentration flux and r.m.s. velocity, respectively.

The second term on the right-hand side of (B3) can be written as

$$\begin{aligned}
 \langle Tu_z \rangle &= \int_0^1 \langle Tu_z \rangle_A dz = \frac{Le}{Ra_S} \int_0^1 \left(Nu_T + \left\langle \frac{\partial T}{\partial z} \right\rangle_A \right) dz = \frac{Le}{Ra_S} \int_0^1 \left(Nu_T + \frac{\partial \langle T \rangle_A}{\partial z} \right) dz \\
 &= \frac{Le}{Ra_S} (Nu_T + \langle T \rangle_{A(z=1)} - \langle T \rangle_{A(z=0)}) = \frac{Le}{Ra_S} (Nu_T - 1).
 \end{aligned}
 \tag{B5}$$

The last term on the right-hand side of (B3) can be written as

$$\begin{aligned}
 \langle Su_z \rangle &= \int_0^1 \langle Su_z \rangle_A dz = \frac{1}{Ra_S} \int_0^1 \left(-Nu_S + \left\langle \frac{\partial S}{\partial z} \right\rangle_A \right) dz = \frac{1}{Ra_S} \int_0^1 \left(-Nu_S + \frac{\partial \langle S \rangle_A}{\partial z} \right) dz \\
 &= \frac{1}{Ra_S} (-Nu_S + \langle S \rangle_{A(z=1)} - \langle S \rangle_{A(z=0)}) = \frac{1}{Ra_S} (-Nu_S + 1).
 \end{aligned}
 \tag{B6}$$

l_r	V_{DP}	L	$N_x(m_x)$	$N_y(m_y)$	$N_z(m_z)$	N_t	Nu_S	Nu_T	u^{rms}
0.1	0.1	4	384(1)	384(1)	192(1)	60	17.76	1.53	0.532
	0.2	4	384(1)	384(1)	192(1)	60	17.56	1.52	0.531
	0.3	4	576(1)	576(1)	192(1)	40	17.61	1.47	0.514
	0.5	4	1536(1)	1536(1)	192(1)	5	16.29	1.28	0.432
	0.6	4	1728(1)	1728(1)	192(1)	4	15.70	1.22	0.449
0.5	0.1	4	384(1)	384(1)	192(1)	60	17.57	1.53	0.539
	0.2	4	384(1)	384(1)	192(1)	60	17.41	1.52	0.546
	0.3	4	384(1)	384(1)	192(1)	40	16.71	1.50	0.558
	0.5	4	768(1)	768(1)	192(1)	20	15.76	1.47	0.638
	0.6	4	1536(1)	1536(1)	192(1)	5	13.33	1.47	0.888
1	0.1	4	384(1)	384(1)	192(1)	60	17.41	1.54	0.542
	0.2	4	384(1)	384(1)	192(1)	60	17.05	1.54	0.559
	0.3	4	384(1)	384(1)	192(1)	40	16.48	1.52	0.599
	0.5	4	768(1)	768(1)	192(1)	20	15.87	1.52	0.686
	0.6	4	1536(1)	1536(1)	192(1)	5	15.12	1.54	0.787

Table 5. Summary of simulations for DDC at $Ra_S = 10^3$ and $Ra_T = 50$ in heterogeneous porous media. Columns from left to right are the correlation length, Dykstra–Parsons coefficient, aspect ratio, resolutions in the x-axis, y-axis, z-axis (with refinement factors for multiple resolutions), non-dimensionalised simulating time, averaged concentration flux, heat flux and r.m.s. velocity, respectively.

Therefore, an analytical relation for the mean velocity square can be obtained as

$$\langle |\mathbf{u}|^2 \rangle = \frac{\Lambda Le}{Ra_S} (Nu_T - 1) + \frac{1}{Ra_S} (Nu_S - 1). \tag{B7}$$

Introducing the Péclet number as

$$Pe = \frac{U_c \sqrt{\langle |\mathbf{u}|^2 \rangle} H}{\kappa_S} = Ra_S \sqrt{\langle |\mathbf{u}|^2 \rangle}, \tag{B8}$$

with $U_c = \bar{K} g \rho_0 \beta_S \Delta S / \mu$, we finally obtain an analytical relation

$$Pe^2 = Ra_S [\Lambda Le (Nu_T - 1) + (Nu_S - 1)]. \tag{B9}$$

REFERENCES

ABRAHAMSEN, P., KVERNELV, V. & BARKER, D. 2018 Simulation of Gaussian random fields using the fast Fourier transform (FFT). In *ECMOR XVI-16th European Conference on the Mathematics of Oil Recovery*, pp. 1–14. European Association of Geoscientists & Engineers.

BACHU, S. 2000 Sequestration of CO₂ in geological media: criteria and approach for site selection in response to climate change. *Energy convers. Manage.* **41** (9), 953–970.

BACHU, S. 2003 Screening and ranking of sedimentary basins for sequestration of CO₂ in geological media in response to climate change. *Environ. Geol.* **44** (3), 277–289.

BHARATH, K.S. & FLYNN, M.R. 2021 Buoyant convection in heterogeneous porous media with an inclined permeability jump: an experimental investigation of filling box-type flows. *J. Fluid Mech.* **924**, A35.

BRAESTER, C. & VADASZ, P. 1993 The effect of a weak heterogeneity of a porous medium on natural convection. *J. Fluid Mech.* **254**, 345–362.

BRIGGS, W.L., HENSON, V.E. & MCCORMICK, S.F. 2000 *A Multigrid Tutorial*, 2nd edn. Society for Industrial and Applied Mathematics.

CAMHI, E., MEIBURG, E. & RUIH, M. 2000 Miscible rectilinear displacements with gravity override. Part 2. Heterogeneous porous media. *J. Fluid Mech.* **420**, 259–276.

CHEN, C., ZENG, L. & SHI, L. 2013 Continuum-scale convective mixing in geological CO₂ sequestration in anisotropic and heterogeneous saline aquifers. *Adv. Water Resour.* **53**, 175–187.

- DE PAOLI, M., PIROZZOLI, S., ZONTA, F. & SOLDATI, A. 2022 Strong Rayleigh–Darcy convection regime in three-dimensional porous media. *J. Fluid Mech.* **943**, A51.
- DE PAOLI, M., ZONTA, F. & SOLDATI, A. 2017 Dissolution in anisotropic porous media: modelling convection regimes from onset to shutdown. *Phys. Fluids* **29** (2), 026601.
- DE VREUZY, J.-R., CARRERA, J., DENTZ, M. & LE BORGNE, T. 2012 Time evolution of mixing in heterogeneous porous media. *Water Resour. Res.* **48** (6), W06511.
- ENNIS-KING, J. & PATERSON, L. 2003 Role of convective mixing in the long-term storage of carbon dioxide in deep saline formations. In *SPE Annual Technical Conference and Exhibition*, p. SPE–84344–MS. SPE.
- FARAJZADEH, R., RANGANATHAN, P., ZITHA, P.L. & BRUINING, J. 2010 The effect of heterogeneity on the character of density-driven natural convection of CO₂ overlying a brine layer. In *SPE Canada Unconventional Resources Conference*, p. SPE–138168–MS. SPE.
- GREEN, C.P. & ENNIS-KING, J. 2014 Steady dissolution rate due to convective mixing in anisotropic porous media. *Adv. Water Resour.* **73**, 65–73.
- GRIFFITHS, R.W. 1981 Layered double-diffusive convection in porous media. *J. Fluid Mech.* **102**, 221–248.
- HEWITT, D.R. 2020 Vigorous convection in porous media. *Proc. R. Soc. A Math. Phys. Engng Sci.* **476** (2239), 20200111.
- HEWITT, D.R., NEUFELD, J.A. & LISTER, J.R. 2012 Ultimate regime of high Rayleigh number convection in a porous medium. *Phys. Rev. Lett.* **108** (22), 224503.
- HEWITT, D.R., NEUFELD, J.A. & LISTER, J.R. 2013 Convective shutdown in a porous medium at high Rayleigh number. *J. Fluid Mech.* **719**, 551–586.
- HEWITT, D.R., NEUFELD, J.A. & LISTER, J.R. 2014 High Rayleigh number convection in a three-dimensional porous medium. *J. Fluid Mech.* **748**, 879–895.
- HILL, A.A. 2005 Double–diffusive convection in a porous medium with a concentration based internal heat source. *Proc. R. Soc. A Math. Phys. Engng Sci.* **461** (2054), 561–574.
- HU, C., XU, K. & YANG, Y. 2023 Effects of the geothermal gradient on the convective dissolution in CO₂ sequestration. *J. Fluid Mech.* **963**, A23.
- HUPPERT, H.E. & NEUFELD, J.A. 2014 The fluid mechanics of carbon dioxide sequestration. *Annu. Rev. Fluid Mech.* **46** (1), 255–272.
- ISLAM, A., KORRANI, A.K.N., SEPEHRNOORI, K. & PATZEK, T. 2014a Effects of geochemical reaction on double diffusive natural convection of CO₂ in brine saturated geothermal reservoir. *Energy Procedia* **63**, 5357–5377.
- ISLAM, A.W., LASHGARI, H.R. & SEPEHRNOORI, K. 2014b Double diffusive natural convection of CO₂ in a brine saturated geothermal reservoir: study of non-modal growth of perturbations and heterogeneity effects. *Geothermics* **51**, 325–336.
- JENSEN, J.L., LAKE, L.W., CORBETT, P.W.M. & GOGGIN, D.J. 1997 *Statistics for Petroleum Engineers and Geoscientists*. Prentice Hall.
- JOUNET, A. & BARDAN, G. 2001 Onset of thermohaline convection in a rectangular porous cavity in the presence of vertical vibration. *Phys. Fluids* **13** (11), 3234–3246.
- KONG, X.-Z. & SAAR, M.O. 2013 Numerical study of the effects of permeability heterogeneity on density-driven convective mixing during CO₂ dissolution storage. *Intl J. Greenh. Gas Control* **19**, 160–173.
- KUZNETSOV, A.V. & NIELD, D.A. 2008 The effects of combined horizontal and vertical heterogeneity on the onset of convection in a porous medium: double diffusive case. *Transp. Porous Med.* **72** (2), 157–170.
- KUZNETSOV, A.V. & NIELD, D.A. 2012 The onset of double-diffusive convection in a vertical cylinder occupied by a heterogeneous porous medium with vertical throughflow. *Transp. Porous Med.* **95** (2), 327–336.
- LAPWOOD, E.R. 1948 Convection of a fluid in a porous medium. *Math. Proc. Camb. Phil. Soc.* **44** (4), 508–521.
- LOMBARDO, S., MULONE, G. & STRAUGHAN, B. 2001 Non-linear stability in the Bénard problem for a double-diffusive mixture in a porous medium. *Math. Meth. Appl. Sci.* **24** (16), 1229–1246.
- MAHYAPOUR, R., MAHMOODPOUR, S., SINGH, M. & OMRANI, S. 2022 Effect of permeability heterogeneity on the dissolution process during carbon dioxide sequestration in saline aquifers: two- and three-dimensional structures. *Geomech. Geophys. Geo-Energy Geo-Resour.* **8** (2), 70.
- MURRAY, B.T. & CHEN, C.F. 1989 Double-diffusive convection in a porous medium. *J. Fluid Mech.* **201**, 147–166.
- NIELD, D.A. 1968 Onset of thermohaline convection in a porous medium. *Water Resour. Res.* **4** (3), 553–560.
- NIELD, D.A. & BEJAN, A. 2017 *Convection in Porous Media*. Springer International Publishing.
- NIELD, D.A. & KUZNETSOV, A.V. 2007a The effects of combined horizontal and vertical heterogeneity and anisotropy on the onset of convection in a porous medium. *Intl J. Therm. Sci.* **46** (12), 1211–1218.
- NIELD, D.A. & KUZNETSOV, A.V. 2007b The effects of combined horizontal and vertical heterogeneity on the onset of convection in a porous medium. *Intl J. Heat Mass Transfer* **50** (9–10), 1909–1915.

- NIELD, D.A. & KUZNETSOV, A.V. 2011 The effects of combined horizontal and vertical heterogeneity on the onset of convection in a porous medium with horizontal throughflow. *Intl J. Heat Mass Transfer* **54** (25–26), 5595–5601.
- NIELD, D.A., KUZNETSOV, A.V. & SIMMONS, C.T. 2010 The effect of strong heterogeneity on the onset of convection in a porous medium: 2D/3D localization and spatially correlated random permeability fields. *Transp. Porous Med.* **83**, 465–477.
- NORDBOTTEN, J.M., CELIA, M.A. & BACHU, S. 2005 Injection and storage of CO₂ in deep saline aquifers: analytical solution for CO₂ plume evolution during injection. *Transp. Porous Med.* **58** (3), 339–360.
- OLIVER, D.S. 1995 Moving averages for Gaussian simulation in two and three dimensions. *Math. Geol.* **27**, 939–960.
- OSTILLA-MÓNICO, R., YANG, Y., VAN DER POEL, E.P., LOHSE, D. & VERZICCO, R. 2015 A multiple-resolution strategy for direct numerical simulation of scalar turbulence. *J. Comput. Phys.* **301**, 308–321.
- OTERO, J., DONTCHEVA, L.A., JOHNSTON, H., WORTHING, R.A., KURGANOV, A., PETROVA, G. & DOERING, C.R. 2004 High-Rayleigh-number convection in a fluid-saturated porous layer. *J. Fluid Mech.* **500**, 263–281.
- PIROZZOLI, S., DE PAOLI, M., ZONTA, F. & SOLDATI, A. 2021 Towards the ultimate regime in Rayleigh–Darcy convection. *J. Fluid Mech.* **911**, R4.
- PRAKASH, J. & GUPTA, S.K. 2012 Characterization of thermohaline convection in porous medium: Brinkman model. *Intl J. Engng Res. Applics.* **2** (6), 1082–1087.
- RANGANATHAN, P., FARAJZADEH, R., BRUINING, H. & ZITHA, P.L.J. 2012 Numerical simulation of natural convection in heterogeneous porous media for CO₂ geological storage. *Transp. Porous Med.* **95** (1), 25–54.
- RAPAKA, S., PAWAR, R.J., STAUFFER, P.H., ZHANG, D. & CHEN, S. 2009 Onset of convection over a transient base-state in anisotropic and layered porous media. *J. Fluid Mech.* **641**, 227–244.
- RIAZ, A. & CINAR, Y. 2014 Carbon dioxide sequestration in saline formations: part I—review of the modeling of solubility trapping. *J. Petrol. Sci. Engng* **124**, 367–380.
- ROSENBERG, N.D. & SPERA, F.J. 1992 Thermohaline convection in a porous medium heated from below. *Intl J. Heat Mass Transfer* **35** (5), 1261–1273.
- RUBIN, H. & ROTH, C. 1979 On the growth of instabilities in groundwater due to temperature and salinity gradients. *Adv. Water Resour.* **2**, 69–76.
- SALIBINDLA, A.K.R., SUBEDI, R., SHEN, V.C., MASUK, A.U.M. & NI, R. 2018 Dissolution-driven convection in a heterogeneous porous medium. *J. Fluid Mech.* **857**, 61–79.
- SLIM, A.C. 2014 Solutal-convection regimes in a two-dimensional porous medium. *J. Fluid Mech.* **741**, 461–491.
- SOBOLEVA, E.B. 2018 Density-driven convection in an inhomogeneous geothermal reservoir. *Intl J. Heat Mass Transfer* **127**, 784–798.
- TAUNTON, J.W., LIGHTFOOT, E.N. & GREEN, T. 1972 Thermohaline instability and salt fingers in a porous medium. *Phys. Fluids* **15** (5), 748–753.
- TENG, Y. & ZHANG, D. 2018 Long-term viability of carbon sequestration in deep-sea sediments. *Sci. Adv.* **4** (7), eaao6588.
- TREVISAN, O.V. & BEJAN, A. 1987 Mass and heat transfer by high Rayleigh number convection in a porous medium heated from below. *Intl J. Heat Mass Transfer* **30** (11), 2341–2356.
- TREVISAN, O.V. & BEJAN, A. 1990 Combined heat and mass transfer by natural convection in a porous medium. In *Advances in Heat Transfer*, vol. 20, pp. 315–352. Elsevier.
- TYVAND, P.A. 1980 Thermohaline instability in anisotropic porous media. *Water Resour. Res.* **16** (2), 325–330.
- VAFAI, K. (Ed.) 2005 *Handbook of Porous Media*, 2nd edn. CRC Press.
- WAGGONER, J.R., CASTILLO, J.L. & LAKE, L.W. 1992 Simulation of EOR processes in stochastically generated permeable media. *SPE Form. Eval.* **7** (2), 173–180.
- WANG, L., NAKANISHI, Y., HYODO, A. & SUEKANE, T. 2017 Three-dimensional finger structure of natural convection in homogeneous and heterogeneous porous medium. *Energy Procedia* **114**, 5048–5057.
- WANG, S. & TAN, W. 2009 The onset of Darcy–Brinkman thermosolutal convection in a horizontal porous media. *Phys. Lett. A* **373** (7), 776–780.
- XU, X., CHEN, S. & ZHANG, D. 2006 Convective stability analysis of the long-term storage of carbon dioxide in deep saline aquifers. *Adv. Water Resour.* **29** (3), 397–407.
- ZHU, X., FU, Y. & DE PAOLI, M. 2024 Transport scaling in porous media convection. *J. Fluid Mech.* **991**, A4.